Statistical study of OB stars in NGC 6334 and NGC 6357

D. Russeil, Annie Zavagno, C. Adami, L. D. Anderson, Sylvain Bontemps, F. Motte, J. A. Rodon, N. Schneider, A. Ilmane, K. J. Murphy

A&A 538, A142 (2012)
DOI: 10.1051/0004-6361/201117299

Astronomy & Astrophysics

Statistical study of OB stars in NGC 6334 and NGC 6357⋆,⋆⋆,⋆⋆⋆

D. Russeil[1], A. Zavagno[1], C. Adami[1], L. D. Anderson[1], S. Bontemps[2], F. Motte[3], J. A. Rodon[1], N. Schneider[3], A. Ilmane[4], and K. J. Murphy[5]

[1] Laboratoire d'Astrophysique de Marseille – UMR 6110, CNRS – Université de Provence, 13388 Marseille Cedex 13, France
e-mail: delphine.russeil@oamp.fr
[2] Laboratoire d'Astrophysique de Bordeaux, OASU – UMR 5804, CNRS – Université de Bordeaux 1, 2 rue de l'Observatoire, BP 89, 33270 Floirac, France
[3] Laboratoire AIM, CEA/DSM – INSU/CNRS – Université Paris Diderot, IRFU/Service d'Astrophysique, CEA-Saclay, 91191 Gif-sur-Yvette Cedex, France
[4] Laboratoire de mathématique Jean Alexandre Dieudonne, UMR 6621 CNRS UNSA – Université de Nice – Sophia Antipolis, 06108 Nice Cedex 02, France
[5] Department of Physics and Astronomy, Ohio University, 251B ClippingerLab, Athens, OH 45701, USA

Received 20 May 2011 / Accepted 8 December 2011

ABSTRACT

Context. Star-forming complexes are large structures exhibiting massive star-formation at different stages of evolution, from dense cores to well-developed H II regions. They are very interesting for the study of the formation and evolution of stars. NGC 6334 and NGC 6357 are two active and relatively nearby star-forming complexes. From the extinction map and the sub-mm cold dust emission, and because they have similar velocities, these regions are most likely connected. However, located in the direction of the Galactic center their radial velocity is not representative of their distance. An alternative is then to determine the distance of NGC 6334 and NGC 6357 from their stellar content.

Aims. Our aim is to perform a census of O-B3 ionising stars in NGC 6334 and NGC 6357, to determine the extinction coefficient, and the distance of both regions. A census of O-B3 stars is an essential basis for estimating the statistical lifetime of the earliest massive star-forming phases.

Methods. We performed a U, B, V, and R photometric survey of a large area covering NGC 6334 and NGC 6357 with the VIMOS (ESO-VLT) and the MOSAIC (CTIO) instruments. This allows us to have a complete census of O to B3 stars up to $V = 22.6$ mag. The OB stars are selected based on their $U - B$ and $B - V$ colors. The most robust extinction coefficient is determined from color–color plots before computing the distance of the OB stars.

Results. We find a higher value than typical of the diffuse interstellar medium for R_V of 3.53 ± 0.08 and 3.56 ± 0.15 for NGC 6357 and NGC 6334, respectively. Adopting these R_V values, the distances of NGC 6357 and NGC 6334 are 1.9 ± 0.4 kpc and 1.7 ± 0.3 kpc. We conclude that, within the error bars, both regions are thus at the same distance of 1.75 kpc (weighted mean). We confirm that the value of R_V is linked to the large dust grain content. In particular, we found that there are more very small grains in NGC 6357 than in NGC 6334, suggesting that NGC 6357 could be more evolved than NGC 6334. Placed in the Galactic context, the NGC 6334-NGC 6357 complex appears to be located at the inner edge of the Sagittarius-Carina arm. Our census of O to B3 stars leads to a count of ∼230, which allows us to determine the statistical lifetime of the earliest phases of the massive stars. The starless and the protostellar phases have a mean statistical lifetime of $\sim 1.5 \times 10^4$ yr and $\sim 2.2 \times 10^5$ yr, respectively.

Key words. H II regions – dust, extinction

1. Introduction

Star-forming complexes are the main building blocks of the large-scale structure of galaxies and major sites to study how massive stars form. However, in contrast to low-mass stars, the formation of high-mass stars remains poorly understood. In this framework, the *Herschel*/HOBYS (PI: F. Motte, A. Zavagno, S. Bontemps) Guaranteed Time Key Programme is performing a 75 to 500 μm SPIRE and PACS imaging of a complete sample of molecular complexes more massive than Orion at distance of less than 3 kpc. This sample has been built based on dust extinction images and CO surveys of the Galactic plane and includes NGC 6334 and NGC 6357.

In our Galaxy, NGC 6334 and NGC 6357 are two very active star-forming complexes seen in the optical as two extensive and intensely star-forming H II regions. The extinction map and the morphology of the 1.2 mm cold dust emission seem to indicate that NGC 6334 and NGC 6357 are connected by a filamentary structure, suggesting that both regions belong to a single complex (Russeil et al. 2010).

The molecular emission associated with NGC 6334 has a mean molecular velocity of $V_{\rm LSR} = -4$ km s^{-1} (Kraemer & Jackson 1999) similar to the value from radio recombination lines, $V_{\rm LSR} = -3.6$ km s^{-1}, of NGC 6357 (Caswell & Haynes 1987). These similar velocities for regions located spatially close to each other indicate that they are both at a similar distance.

⋆ Based on observations made with the VIMOS instrument at the VLT-ESO. Based on visiting astronomer observations, at Cerro Tololo Inter-American Observatory, National Optical Astronomy Observatory, which is operated by the Association of Universities for Research in Astronomy, under contract with the National Science Foundation.

⋆⋆ Appendices are available in electronic form at http://www.aanda.org

⋆⋆⋆ Full Tables A.1 and A.2 are only available at the CDS via anonymous ftp to cdsarc.u-strasbg.fr (130.79.128.5) or via http://cdsarc.u-strasbg.fr/viz-bin/qcat?J/A+A/538/A142

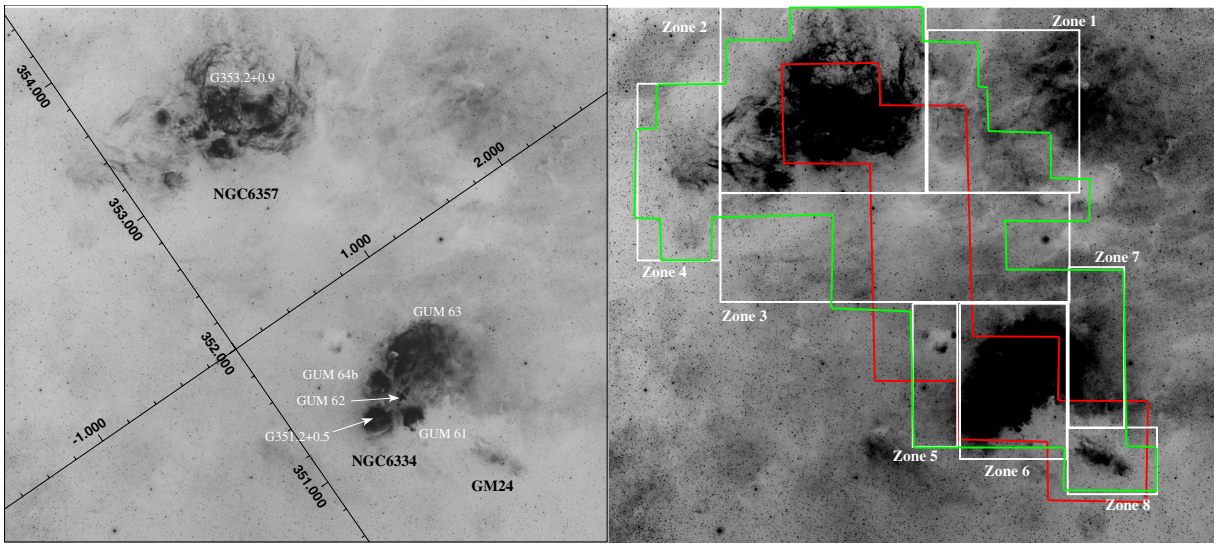

Fig. 1. a) Hα image (UKST Hα survey, Parker et al. 2005) of the H II regions NGC 6334 and NGC 6357 (Galactic coordinates). **b)** Hα image with overplotted the coverage of the VIMOS observations (green) and CTIO observations (red), as well as the zones 1 to 8 (white) discussed in the text. Zones 2, 6, and 8 correspond respectively to NGC 6357, NGC 6334, and GM 24.

Independant distance determinations of each region are not yet well-established. Owing to their Galactic coordinates close to the Galactic center direction, l, b = 351.16°, +0.69° and l, b = 353.01°, +0.89°, respectively, for NGC 6334 and NGC 6357, the kinematic distance is unreliable. The best way to derive their distances is from the determination of the distance to their exciting stars.

As reviewed by Persi & Tapia (2008), NGC 6334 (=Sharpless 8 = RCW 127) contains the H II regions (Fig. 1) GUM 61, GUM 62, GUM 63, and GUM 64 (Gum 1955) and G351.2+0.5. Roslund (1966), Neckel (1978), Walborn (1982), and Persi & Tapia (2008) computed the distance to NGC 6334 from the distances to the visible early-type stars in these H II regions and obtained d = 1.45 kpc, 1.74 kpc, 2.30 kpc and 1.61 kpc, respectively. Persi & Tapia (2008) underlined that the discrepancies are due to the different adopted M_V calibrations and the adopted extinction law (R_V value).

In the optical, NGC 6357 exhibits several bubbles and shell-like regions. The brightest H II region (G353.2+0.9) shows a sharp boundary facing the massive open cluster Pismis 24. The distance of NGC 6357 is usually established from the distance of Pismis 24 (the exciting cluster of NGC 6357); its most recent determination was that of Massey et al. (2001), who give a value of 2.5 kpc. This distance differs from the 1.7 kpc suggested by Neckel (1978) and Lortet et al. (1984) and the 1.1 kpc and 1.74 kpc derived by Conti & Vacca (1990) and Van der Hucht (2001), respectively, for the Wolf-Rayet star HD 157504 (WR 93).

The distance of NGC 6334 and NGC 6357 has therefore not yet been well-established. However, since the distance is an essential parameter for the determination of the mass, size, and luminosity of the associated young objects (e.g. Russeil et al. 2011), it is essential to evaluate in an homogenous way the distance of the early-type stars in the direction of NGC 6334 and NGC 6357. In this paper, we focus on the content of ionizing OB stars of the star-forming complexes NGC 6334 and NGC 6357 to more tightly constrain their distances, to place them in the Galactic context, and to perform a census of their OB stars.

2. Observations and data extraction

2.1. U, B, and V VIMOS data

We observed NGC 6334, NGC 6357, and GM 24 (GM 1-24, Gyulbudaghian et al. 1977) in U, B, and V bands with the VIMOS camera (ESO-VLT). VIMOS is a visible (360 to 1000 nm) wide field imager and multi-object spectrograph mounted at the Nasmyth focus B of UT3 Melipal. We use VIMOS in its imaging mode. This led to the observation of 67 fields, each composed of 4 quadrants of 7′ × 8′ separated by 2′ gaps. The coverage is presented in Fig. 1. The typical observing method was three exposures of 3 s in B, seven exposures of 4 s in U, and four exposures of 3 s in V. The observations were taken in service mode and delivered flatfielded, bias-corrected and with calculated astrometric and photometric data (zero point, extinction coefficient).

We extracted stellar positions and magnitudes using SExtractor (Bertin & Arnouts 1996). We kept objects a with SExtractor flag ≤3 (such a condition ensures a good photometry and excludes saturated objects). In addition, we excluded data at the borders of the CCD and in dead columns. All objects brighter than V = 10 mag were typically saturated. As we treated the image independently, we performed a cross-correlation between the extracted U, B, and V data in order to establish a catalogue of stars with U, B, and V magnitudes.

We measured the completeness as in Adami et al. (2006) and Durret et al. (2010). This method adds artificial stars of different magnitudes and at different locations to the original images and then attempts to recover them by running SExtractor again with the same parameters used for object detection and classification on the original images. We investigated the completeness from three typical images located at different parts of the surveyed area with varying levels of background and source crowding. The 90% mean completeness level (Fig. 2) is respectively 21.8, 22.4, and 22.6 mag for U, B, and V filters. Figure 2, shows how the completeness levels vary from CCD to CCD because of the quantum efficiency variations between individual CCDs and because of fluctuations in the diffuse background light.

From a statistical study of the zero-point, we estimated dispersions of 0.09 mag for U, 0.04 mag for B, and 0.03 mag for V.

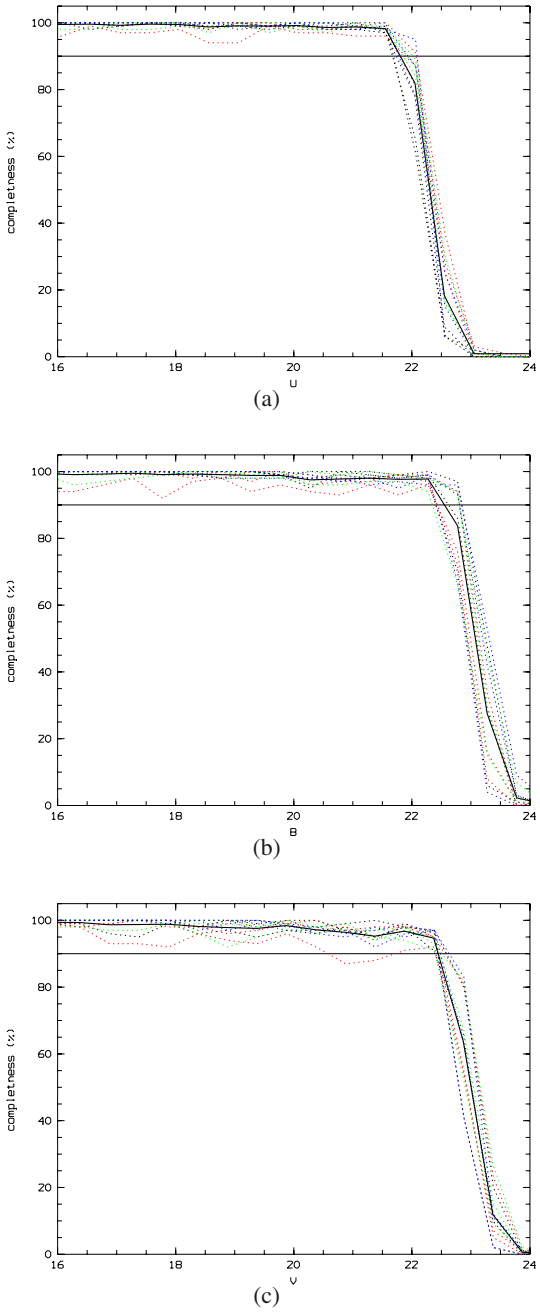

(a) (b) (c)

Fig. 2. *U* **a)**, *B* **b)**, and *V* **c)** completeness level in individual CCDs (each dotted curve corresponds to a CCD quadrant, and the black curve is the average of these dotted curves) for the fields centered respectively at $17^h20^m10\overset{s}{.}0$; $-35°57'18\overset{''}{.}0$ (NGC 6334, blue), $17^h22^m09\overset{s}{.}0$; $-35°03'06\overset{''}{.}0$ (green), and $17^h25^m37\overset{s}{.}0$; $-34°13'27\overset{''}{.}3$ (NGC 6357, red).

The delivered photometric calibration neglects the color term. Thus we estimated the typical error caused by this assumption about the mean color coefficient estimated for the VIMOS instrument and the mean color of OB stars. This leads to a typical error of 0.017 mag in *U* and *B* and 0.006 mag in *V*. We then estimated the error in the magnitude of a star to be the quadratic sum of the magnitude errors given by SExtractor, the zero-point uncertainty, and the color term uncertainty. This led to typical errors of 0.04 mag, 0.09 mag, and 0.23 mag, respectively, in *V*, *B*, and *U*.

Finally, as some fields overlap, we identified the objects counted twice and retained those located closer to the field center. For the purpose of locating O and B stars, we kept stars with magnitude values in the three (*U*, *B*, and *V*) bands. This provided a sample of 30 388 stars (*U*, *B*, and *V* magnitudes are presented in Appendix, Table A.1).

2.2. R band CTIO images

We obtained R images of NGC 6334, NGC 6357, GM 24, and the more diffuse area between NGC 6334 and NGC 6357 with the MOSAIC camera (Blanco-CTIO). This instrument is an eight CCD mosaic imager with a pixel scale of 0.27″ mounted at the prime focus of the 4-m Blanco telescope at the Cerro Tololo Inter-American Observatory (CTIO). These observations consist of six fields composed of three exposures of 10 s each. The global coverage is presented Fig. 1. Each field consists of eight quadrants (separated by gaps of ∼13″ in rows and ∼9.5″ in columns) covering a $36' \times 36'$ field of view. The bias and the flat-field corrections were applied to each of the eight CCD images independently, while the combination of the different exposures, the astrometry, the reconstruction of the final image and the construction of the weight images were done with the modules MissFITS, SCAMP, and SWarp of TERAPIX (Bertin et al. 2002). The photometric calibration was performed using the observation of the Landolt calibration stars S107a, S107b, S104, and S98 (Landolt 2009), giving an extinction coefficient of 0.095 ± 0.043 mag and a zero point of 25.57 ± 0.02 mag. The extraction of the stellar positions and magnitudes was done using SExtractor with the weight images produced by the SWarp module. We kept only objects with a SExtractor flag below 3, and excluded stars in the borders of the CCD and in dead columns. This provided a sample of 53 420 stars (the *R* magnitudes of which are presented in Appendix, Table A.2). The estimated saturation limit is 11 mag and the typical magnitude uncertainty (quadratic sum of the magnitude errors given by SExtractor, the zero-point uncertainty, and the extinction coefficient uncertainty) is 0.05 mag.

3. Other available data sets

3.1. Near-Infrared data from 2MASS

To complement our optical data, we used data from the Two Micron All Sky Survey (2MASS) point source catalog (Skrutsie et al. 2006). The 2MASS survey scanned the entire sky uniformly in three near-IR bands: *J* (1.25 μm), *H* (1.65 μm), and K_S (2.17 μm). The 2MASS point source catalog[1] (Skrutsie et al. 2006) consists of accurate positions (astrometric accuracy rms better than 200 mas) and brightness information for over 400 million point sources. The point source catalog is more than 99% complete for magnitudes of $J < 15.8$, $H < 15.1$, and $K_S < 14.3$ mag. The photometric signal-to-noise ratio is >10 (i.e. $\sigma_{J,H,K_s} \leq 0.1$ mag) for sources brighter than the completeness limits. The typical magnitude error is 0.05 mag, 0.06 mag, and 0.05 mag, respectively in *J*, *H*, and K_S.

3.2. DENIS data

The DENIS[2] imaging survey (Epchtein et al. 1997) gives a nearly complete overview of the southern sky in three NIR bands: Gunn-*I* (0.85 μm), *J* (1.25 μm), and K_S (2.15 μm). The images have been taken simultaneously in all three bands, which

[1] http://irsa.ipac.caltech.edu/

[2] Point source catalog available from http://irsa.ipac.caltech.edu/

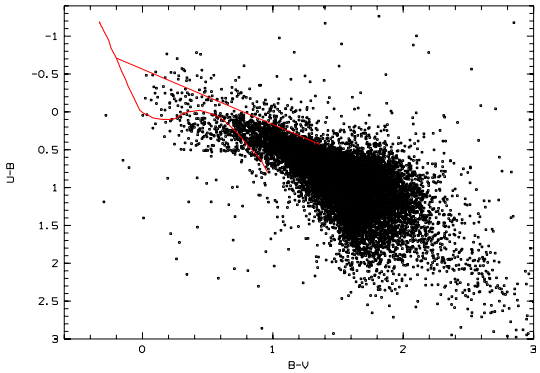

Fig. 3. Color−color diagram for stars with U, B, and V magnitudes. The red curve is the theoretical unreddened main-sequence and the line is the standard reddening vector, up to $A_V = 5$ mag, for a B3V star (from Schimdt-Kaler 1983).

leads to a very high accuracy in the colors of the objects independent of photometric errors. The DENIS data have a positional accuracy better than 2″ and the magnitude limits are 18.5 mag, 16.5 mag, and 14 mag in I, J, and K_S, respectively. The typical magnitude uncertainty is 0.15 mag, 0.11 mag and 0.10 mag in J, K_S, and I, respectively.

3.3. USNO-B1.0 data

USNO-B is an all-sky survey obtained from scans of 7435 Schmidt plates taken for the various optical sky surveys during the past 50 years. The USNO-B1.0 is complete down to $V = 21$ mag, has an astrometric accuracy of 0.2″, and a photometric accuracy of 0.3 mag (Monet et al. 2003). From the point source catalog[3] we extracted R and I magnitudes.

4. The O-B3 star sample

We selected the young and massive stars (O to B3 stars) based on their $U - B$ and $B - V$ colors. The interstellar reddening affects the intrinsic $U-B$ and $B-V$ colors following the reddening line that has the form: $E_{U-B}/E_{B-V} = X + YE_{B-V}$. In this equation, E_{U-B} and E_{B-V} are the color excesses, X is the slope of the reddening line, and Y is the curvature term. We used the reddening path $E_{U-B}/E_{B-V} = 0.72 + 0.05E_{B-V}$ (Schmidt-Kaler 1983). To select O to B3 stars from the $U - B/B - V$ color−color diagram, we selected stars above the reddening path of a B3 star (Fig. 3). Following Turner (1996), this corresponds to a normal extinction law ($R_V = 3.1$), while larger R_V (as expected for star-forming regions) seem to induce a shallower slope. This does not impact our selection process as stars following a reddening law with a shallower slope will be above the adopted reddening path. In addition the reddening path does not depend strongly on the adopted intrinsic colors. To test this aspect we plot E_{U-B} versus E_{B-V} for stars with known spectra (Table 2) and fitted the $E_{U-B}/E_{B-V} = X + YE_{B-V}$ relationship for the Schmidt-Kaler (1983) and for the most recent Martins et al. (2006) color calibrations of O stars. If our small sample does not allow us to constrain reliably X and Y, the fit results are similar for both calibrations (with a smaller than 1% difference in X and Y). However, Turner (1989) showed that the slope of the UBV reddening line varies from one region of the Milky-Way to another over a range of at least $X = 0.62$ to 0.80. If the slope is steeper than 0.72, this can cause us to miss some B3 stars.

This provided a sample of 2394 candidate OB stars. We then searched for objects associated with the 2394 candidate OB stars in the DENIS, 2MASS, and USNO catalogues using a 5″ circular cone search radius. We identified 2148 OB stars with a 2MASS counterpart.

From the O-B3 star sample we discuss, in the next section, the extinction law (Sects. 5.1 and 5.2) in connection with the dust properties (Sect. 5.3), the Galactic structure (Sect. 5.4) and the OB stars census (Sect. 5.5).

5. Discussion

5.1. Extinction law

The radiation from massive OB stars can modify the interstellar grains present in their immediate vicinity, hence affect the global interstellar extinction law (e.g. Chini & Wargau 1990; Pandey et al. 2000). Any change in the interstellar law will affect the local extinction and thus the photometric distance determination. Many investigations (e.g. Wegner 1994; Whittet & vanBreda 1980; Rieke & Lebofsky 1985) have shown that the normal extinction law ($R_V = 3.1$) is valid nearly everywhere in our Galaxy, although some exceptions are noted especially in the direction of star-forming regions and open clusters, where the R_V value is higher (e.g. O'Dell & Wen 1992). Different R_V values relate to different environmental conditions and thus different grain-size distributions and compositions, since the extinction depends on the optical properties of the dust grains (e.g. Whittet 2003; Mazzei & Barbaro 2011). In particular low-R_V values are expected arise along the lines of sight to smaller grains.

There are four main methods for determining the extinction and the extinction law in a given direction:

1. The spectro-photometric method, which is based on the comparison of the observed energy distribution of a star of known spectral type with its non-reddened distribution (e.g. Cardelli 1989).
2. The Paschen-Balmer lines ratio method, which uses the comparison between the predicted and observed Paschen-Balmer line pair ratio emitted by the H II regions (e.g. Greve 2010).
3. The color excess method, which uses two color-excess diagrams of the form $E(\lambda - V)$ versus $E(B - V)$ (where λ is one of the wavelengths of a broad band filter) of a group of stars and requires the spectral type, hence the intrinsic color, of observed stars to be known ("method A" of Pandey et al. 2003).
4. The photometric method, which uses two color diagrams (TCDs) of the form $(\lambda - V)$ versus $(B - V)$ (where λ is one of the wavelengths of a broad-band filter) of a group of stars and assumes that the observed stars are main sequence stars ("method B" of Pandey et al. 2003). In these plots, the reddening path coincides with the unreddened main sequence causing the stars of different spectral types and extinctions to form a linear relation parallel to the reddening line. The slope of this distribution, relative to the expected slope for the normal reddening path, allows one to derive the value of R_V.

As we are performing a statistical study of OB stars in the direction of NGC 6334-NGC 6357 and have no spectral information about the stars, the last method is the most appropriate. To investigate the value of R_V in the direction of NGC 6334 – NGC 6357, we used TCDs with λ as one of the wavelengths of the broad band filters (R, I, J, H, K). These TCDs provide an effective method for separating the influence of the normal extinction produced by the diffuse interstellar medium from that of the abnormal extinction. In these diagrams, the slope of the distribution,

[3] Available from http://irsa.ipac.caltech.edu/

Table 1. R_V results.

Zone:	1	2 NGC 63357	3	4	5	6 NGC 6334	7	8 GM24
R_V:	3.32 ± 0.12	3.53 ± 0.08	3.44 ± 0.07	3.37 ± 0.03	3.46 ± 0.06	3.56 ± 0.15	3.16 ± 0.08	3.89 ± 0.09

Table 2. Stellar data available in literature for NGC 6357 (Pismis 24) and NGC 6334.

Name	Equatorial coordinates J2000 (h m s ° ′ ″)	V mag	$B-V$ mag	$U-B$ mag	Spectral type	$V-K_S$ mag	$J-H$ mag	$H-K$ mag	R_V	d kpc	A_V mag
					NGC 6357						
HDE319718 = Pis24-1	17 24 43.41 −34 11 56.5	10.43	1.45	0.40	O3 If*	4.538	0.551	0.283	3.37*	1.65	5.75
HD 157504 = WR93	17 25 08.79 −34 11 12.1	11.46	1.15		WC7(+abs?)	5.595	0.503	0.668	–	–	–
Pis24-17	17 24 44.70 −34 12 02	11.84	1.49	0.28	O3 III(f*)	4.865	0.535	0.306	3.52*	2.03	6.39
Pis24-2	17 24 43.20 −34 12 43.5	11.95	1.41	0.32	O5.5 V((f))	4.260	0.475	0.307	3.27	1.90	5.99
Pis24-15*	17 24 28.86 −34 14 50.3	12.44	1.18	0.26	O8 V	3.974	0.450	0.235	3.38	2.71	5.01
Pis24-13*	17 24 45.68 −34 09 39.2	12.32	1.33	0.22	O6.5 V((f))	4.784	0.574	0.289	3.47	2.08	5.74
Pis24-3*	17 24 42.21 −34 13 21.0	12.77	1.44	0.35	O8 V	4.279	0.524	0.298	3.30	1.92	6.09
Pis24-8*	17 24 38.81 −34 14 58.2	12.95	1.55	0.42		4.460	–	0.208	–	–	–
Pis24-10	17 24 35.94 −34 13 59.9	12.96	1.50	0.38	O9 V	4.272	0.487	0.276	3.31	1.66	6.33
Pis24-16	17 24 44.30 −34 12 00	13.02	1.60		O7.5 V	5.649	0.592	0.490	3.76	–	–
Pis24-7	17 24 47.81 −34 15 16.5	13.46	1.68	0.58		5.036	0.608	0.327	–	–	–
Pis24-12	17 24 42.22 −34 11 41.1	13.88	1.47	0.38	B1 V	4.097	0.508	0.208	3.07	1.51	6.19
Pis24-4	17 24 40.39 −34 12 05.9	13.93	1.43	0.53		4.792	0.595	0.315	–	–	–
Pis24-18	17 24 43.20 −34 11 42	13.97	1.48		B0.5 V:	4.998	0.683	0.341	3.61	–	–
Pis24-9	17 24 39.29 −34 15 26.4	14.26	1.40	0.40		4.258	0.490	0.288	–	–	–
Pis24-11	17 24 34.68 −34 13 17.1	14.53	1.57	0.30		4.741	0.660	0.296	–	–	–
Pis24-19	17 24 43.50 −34 11 41	14.43	1.39		B1 V	4.818	0.592	0.467	3.71	–	–
					NGC 6334						
CD-35 11146	17 19 07.5 −35 37 46	11.44	0.76	−0.04	B2IV	2.05	0.24	0.09	2.98	1.59	3.48
HD319701	17 19 16.0 −35 54 08	10.10	1.08	0.04	B1Ib	3.14	0.37	0.21	3.19	1.73	4.65
HD39699	17 19 30.4 −35 42 36	9.63	0.77	−0.24	O5V((f))	2.29	0.22	0.15	3.37	1.75	3.78
CD-3511477	17 20 05.0 −35 56 38	11.11	0.90	−0.03	B0.5V	2.46	0.27	0.09	3.05	1.4	4.12
HD319697	17 20 24.8 −35 42 32	10.33	0.66	−0.24	B1V	1.62	0.18	0.04	2.84	1.10	3.28
CD-35 11482	17 20 26.5 −35 44 07	10.70	0.73	−0.25	B0.5Ve	3.42	0.38	0.43	4.58	1.41	3.61
CD-35 11483	17 20 33.6 −36 06 26	11.65	1.03	−0.10	B1e	2.53	0.30	0.19	2.80	–	–
HD319703B	17 19 45.0 −36 05 47	11.20	1.25	0.04	O6.5V((f))	3.61	0.28	0.28	–	1.26	5.64
HD319703A	17 19 46.2 −36 05 52	10.71	1.14	0.04	O7III	3.66	0.38	0.27	3.58	1.78	5.12
CD-35 11484	17 20 49.8 −35 52 21	11.33	0.95	0.04	B1V	2.73	0.27	0.18	3.17	1.10	4.27
HD319702	17 20 50.6 −35 51 46	10.13	0.90	0.04	O8III((f))	2.71	0.31	0.17	3.43	2.11	4.03
HD156738	17 20 52.7 −36 04 21	9.37	0.86	−0.14	O6.5III((f))	2.58	0.26	0.16	3.55	1.58	4.05

Notes. Spectral types are from Massey et al. (2001) for NGC 6357 and from Persi & Tapia (2008) and Pinheiro et al. (2010) for NGC 6334. Asterisk following the name in Col. 1 means that U, B and V data are from this paper. Asterisk following value in the R_V column means the data are from Bohigas et al. (2004). JHK_S data are from 2MASS. Distance and A_V were calculated from the R_V of 3.56 and 3.53 for stars in NGC 6334 and NGC 6357, respectively.

m_{obs}, is compared to the theoretical slope, m_{normal} (Pandey et al. 2003). To derive the value of R_V, we used the relation (see Samal et al. 2007; Pandey et al. 2000)

$$R_V = (m_{obs}/m_{normal}) \times R_{normal}, \quad (1)$$

where $R_{normal} = 3.1$.

To investigate the R_V value in NGC 6334-NGC 6357, we divided the area into eight zones based on the individual region (see Fig. 1) and plotted the TCDs for each zone. Zones 2, 6, and 8 encompass NGC 6357, NGC 6334, and GM24 respectively. Zone 3 is the area between NGC 6357 and NGC 6334. Zones 4 and 1 and zones 5 and 7 are on the eastern and western borders of NGC 6357 and NGC 6334, respectively.

Before plotting the TCDs, we adopt the following selection criteria for our sample:

1. We removed IR-excess objects based on their 2MASS $J-H$ and $H-K$ colors. Following Hanson et al. (1997), we kept stars with $(J-H) - (1.83 \times (H-K) + 0.15) \geq 0$.
2. We kept only stars with $V < 21$ mag (to ensure completness) and with $B-V$ uncertainties <0.15 mag.
3. For CTIO data we retained stars with $V-R$ uncertainties ≤0.15 mag.
4. For the 2MASS and DENIS data, we kept stars with magnitude uncertainties ≤0.15 mag and magnitudes brighter than the magnitude limits (see Sects. 3.1 and 3.2).

These criteria helped to minimize the incompleteness problem. For USNO data, we adopted an uncertainty of 0.3 mag for R and I.

In the TCDs, the data were fit using a 1σ-clipping linear regression (see in Appendix B, Figs. B.1 to B.8), and the results are given in Table 1 (the details of the linear regressions and the R_V determination are given in Appendix B). To illustrate our results, we present in Fig. 4 some representative color−color diagrams (all the plots are presented in Appendix). In these plots, the majority of the stars follow a linear distribution. Few stars are located above the general trend. Metallicity or age variations cannot explain this result, because a metallicity effect corresponds to

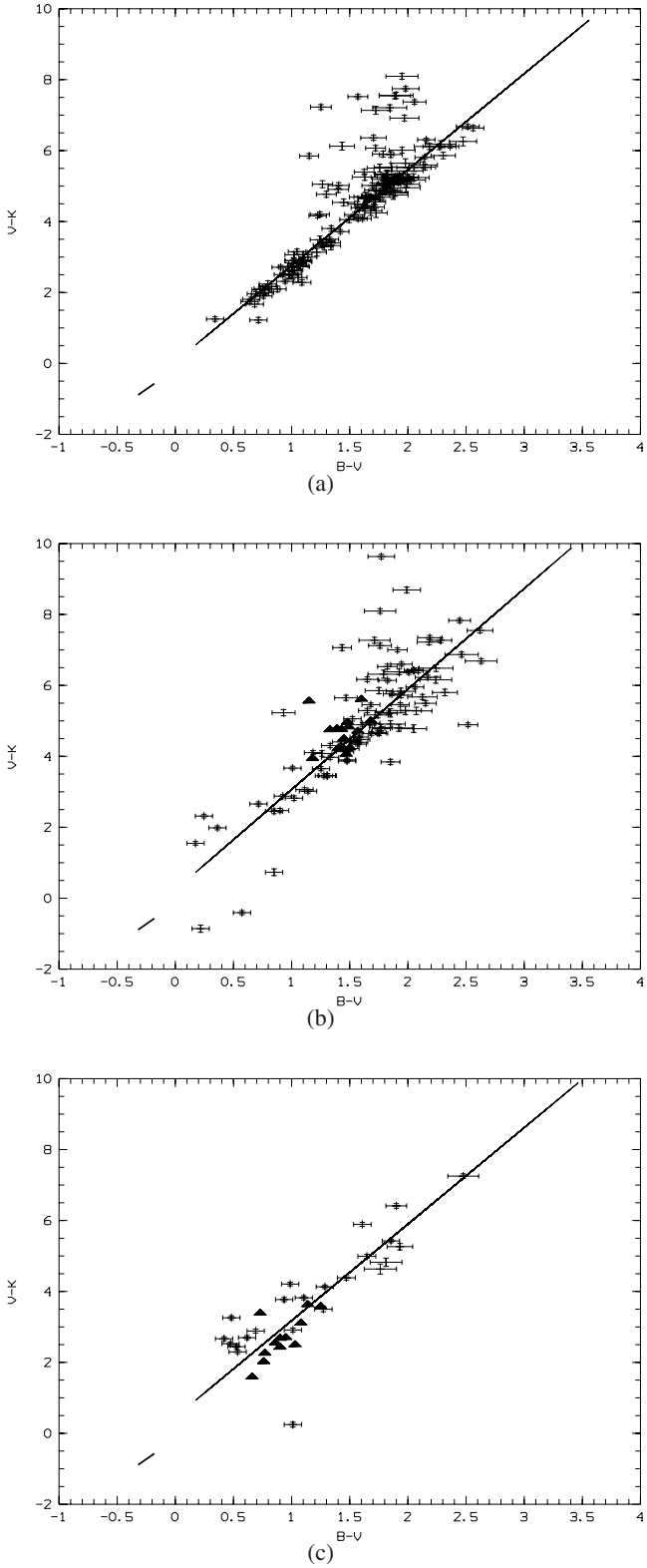

Fig. 4. $V - K$ versus $B - V$ for zone 4 **a)**, zone 2 = NGC 6357 **b)**, and zone 6 = NGC 6334 **c)**. The stars identified spectroscopically (see Sect. 5.2) are also overplotted (filled triangles). The small thick segment on the bottom left of the plots is the locus of the unreddened O-B3 stars (from Martins et al. 2006; Koornneef et al. 1983; and Wegner 1994).

a color variation smaller than 0.1 mag (De Grijs et al. 2001) and an age variation can be represented as isochrones parallel to the reddening vector in color−color diagrams (Leitherer 1999). The most likely explanation is the mis-association with near-infrared data. As expected, this effect is more important in crowded areas such as zone 4, which is the closest to the Galactic plane. In the distribution of the stars, we can delineate overdensities (which are clearly illustrated in Fig. 4a). These provide information about the number of the extinction layers present along the line of sight. In the TCD of zone 4, the lowest Galactic latitude zone, we can distinguish up to four extinction layers centered on $(B - V) \sim 0.7$, 1, 1.3, and 1.75. Stars are mainly located around $(B - V) = 1.5$ and $(B - V) = 1$, respectively, in zones 2 (NGC 6357) and 6 (NGC 6334), underlining the small extinction difference between both regions. Finally, in zones 2, 6, and 7 we note the small number of stars around and below $(B - V) = 0.5$ that depart from the general trend. These stars are probably very nearby foreground stars.

We note that R_V varies from zone to zone. From our data we, confirm a higher value of R_V in NGC 6357 and NGC 6334 than normal extinction. The value of R_V is respectively 3.53 ± 0.08 and 3.56 ± 0.15 for NGC 6357 and NGC 6334, which is very similar for both regions. Neckel & Chini (1981) found a mean value of R_V of 3.8 for NGC 6357-NGC 6334 using a similar method. This value comes from $(R - V)$ versus (vs.) $(B - V)$ and $(I - V)$ vs. $(B - V)$ plots (giving $R_V = 4.08$ and 3.64, respectively) only and using stars in both NGC 6357 and NGC 6334. Considering the same plots, the Neckel & Chini (1981) results are consistent with ours (see Table B.3). Bohigas et al. (2004) found that for Pismis 24 (NGC 6357) $R_V = 3.51$, and Pinheiro et al. (2010) found that $\langle R_V \rangle = 3.5$ for stars in NGC 6334.

The largest value, $R_V = 3.89 \pm 0.09$, is found for zone 8 corresponding to GM24. The zones outsides the H II regions but closer to the Galactic plane (zones 3, 4, and 5) exhibit a similar R_V, around 3.43, which is, despite the more diffuse aspect of the interstellar medium expected in these zones, and is higher than the normal value. The zones at higher Galactic latitude (zones 1 and 7) exhibit a closer-to-normal R_V with a mean value of 3.25.

5.2. Stars with known spectra

The extinction parameters R_V and A_V can also be determined for stars of known spectral type. This can then be compared with our pure photometric approach. We compiled in Table 2 from the literature all the O and B stars in NGC 6334 and NGC 6357 with a known spectral type. In this table, Cols. 1 to 3 and 7 give the name, the coordinates, and the spectral type of the stars, while Cols. 4 to 6 and 8 to 10 give the *UBVJHK* photometric information. Column 11 gives the R_V value deduced from Eq. (2) (see below), while the last two columns give the distance and the extinction for each star calculated with the photometric R_V value determined in the previous section.

Moffat & Vogt (1973) obtained photometry of 15 stars in Pismis 24, for which 12 are members. Massey et al. (2001) obtained spectroscopy of 11 stars, four of which were not in the list of Moffat & Vogt (1973). They found that two of the cluster stars are of type O3, one of which is a supergiant (HDE 319718 = Pis 24-1) and the other appears to be a giant (Pis 24-17). On the basis of the 10 stars with reliably determined luminosity classes, Massey et al. (2001) inferred a distance modulus of 12.03 ± 0.14 mag. When they used only the six O dwarfs to derive the distance, they computed 11.99 ± 0.05 mag. They adopted a distance modulus of 12.0 mag corresponding to a distance of 2.5 kpc, which is larger than the 1.7 kpc suggested by Neckel (1978) and Lortet et al. (1984). The cluster also contains the Wolf-Rayet star HD 157504 (WR 93), which is of type WC7.

Conti & Vacca (1990) described this star as a "WCE + abs" and derived a distance of 1.1 kpc.

In contrast to NGC 6357, NGC 6334 is ionized by a small number of lightly reddened OB stars (Table 2) that are spread about the whole nebula. Persi & Tapia (2008) summarized the available stellar data for early-type stars in the region. NGC 6334 is a grouping of the well-known HII regions GUM 61, GUM 62, GUM 63, and GUM 64. The exciting stars of GUM 61 (HD319703A and HD319703B) and GUM 62 (HD156538) can be clearly distinguished, while the stars HD319702 and CD-35 11484 appear as possible exciting stars of GUM 64.

In GM24, no optical exciting star has been identified. However, a small cluster dominated by a few young massive stars lies at its core (Tapia et al. 1991). On the near-infrared photometry of the cluster stars and extinction considerations, Tapia et al. (1991) deduced a distance of 2 kpc.

Following Samal et al. (2007), one way to estimate the value of R_V is to use stars of known spectral type (Table 2). The R_V value toward a star can be evaluated using the empirical relationship established by Whittet et al. (1976)

$$R_V \simeq 1.1E(V-K)/E(B-V). \quad (2)$$

Equation (2) is based on the finding that the ratio $A_V/E(V-K) \simeq 1.1$ does not change appreciably with the R_V value and across the Galaxy (Whittet & van Breda 1978, 1980). To apply Eq. (2), we transformed the JHK_S magnitudes of the stars from the 2MASS system to the Koornneef system (Koornneef 1983) using the relation given by Carpenter (2001). Intrinsic $(V-K)_0$ colors were taken from Koornneef (1983) and intrinsic $(B-V)_0$ colors from Schmidt-Kaler (1983). The results are listed in Table 2. From these results, we note that R_V varies from place to place on a typical spatial scale that is smaller than our zone size. In this way, Pismis 24 (NGC 6357) exhibits a mean $R_V = 3.43$, while $R_V = 3.42$ for stars associated with NGC 6334. These results are slightly smaller than, but in agreement with, those obtained from the photometric approach ($R_V = 3.53 \pm 0.08$ and 3.56 ± 0.15 in the direction of NGC 6357 and NGC 6334 respectively).

From our photometric determination of R_V, we found for NGC 6357 and NGC 6334 a mean distance of 1.93±0.36 kpc and 1.72 ± 0.26 kpc, respectively, and a mean A_V of 5.93 ± 0.49 mag (Bohigas et al. 2004, give for Pismis 24 $A_V = 6.37$ mag) and 4.52 ± 0.68 mag, respectively. Fang et al. (2011), from isochrone fitting of O stars in Pismis 24, found a distance of 1.7 ± 0.2 kpc and a median extinction of 5.3 mag. We can then conclude that NGC 6334 and NGC 6357 are at an average distance of 1.75 kpc (weighted mean).

5.3. General dust properties

Small values of R_V are generally assumed to relate to a prevalence of small dust grains, which affects the extinction curve at ultraviolet to optical wavelengths (Fitzpatrick 2004). A change in the size distribution naturally explains the variation of R_V in different interstellar media. In particular, any change in the distribution of big grains, with a size of between 15 nm and 100 nm, is expected to be directly related to a change in R_V. The size distribution of big grains can be altered by shock waves (Jones et al. 2005). High-velocity shocks affect grains through sputtering, which reduces the number of small particles, while in shocks with lower velocities, grain-grain collisions alter the size distribution by increasing the small-to-large grain size ratio (Mazzei & Barbaro 2008). Heiles et al. (1988) proposed that shock velocities of at least ~30 km s^{-1} are required to modify the grain size distribution. Seab & Shull (1983) found significant grain destruction only for shock velocities above ~40 km s^{-1}. They predicted that large grains, with sizes larger than 500 Å (the grains that produce most of the 100 μm radiation), are preferentially affected.

To investigate this finding in terms of the value of R_V, we evaluated the average infrared (12, 25, 60, and 100 μm) fluxes (background subtracted) from IRIS[4] in the different zones. The MIPSGAL 24 and 70 μm images (Carey et al. 2009) cannot be used because most of the HII regions are saturated. However, IRAS data facilitates the comparison with dust models similar to those of Désert et al. (1990). The IRAS mean fluxes and their uncertainty are measured from the calibrated images within each area using the ds9-"Funtools" tool. The fluxes are corrected from a background value taken at the same location, on the north-west border (to minimize the contribution of the Galactic plane), in every 12 to 100 μm image.

As expected from Hα emission and OB star content, and based on a large $I(60)/I(100)$ and low $I(12)/I(25)$ ratio corresponding to an increase in the intensity of the radiation field (Boulanger 1988), zones 2, 6, and 8 (corresponding, respectively, to the HII regions NGC 6357, NGC 6334, and GM24) clearly exhibit a stronger radiation field than other zones (Fig. 5). However, NGC 6334 appears to have a higher radiation field than NGC 6357, while NGC 6357 contains more O-type stars (Table 2) and has a higher radio flux than NGC 6334 (see Sect. 4.6).

To characterise the dust properties, we determined the ratios of mid-infrared to far-infrared emission (defined as X1 = $\nu I(12\ \mu\text{m})$ / $[\nu I(60\ \mu\text{m}) + \nu I(100\ \mu\text{m})]$ and X2 = $\nu I(25\ \mu\text{m})$ / $[\nu I(60\,\mu\text{m}) + \nu I(100\,\mu\text{m})]$). These ratios are tools for probing the content of small grains such as PAHs (polycyclic aromatic hydrocarbons) and VSGs (very small grains) relative to big grains (Désert et al. 1990). In particular, X1 depends primarily on the abundance of small particles such as the PAHs. Figure 5 presents the variation in X1 and X2 with R_V. Both X1 and X2 have values similar to those in Désert et al. (1990) for HII regions.

Globally, X1 shows no trend relative to R_V, which is consistent with R_V depending on big grains, but also on the radiation field. When we assumed that zone 3 is the most representative of the typical dust properties, as it is the least affected by HII regions and star formation, we found that the zones 1, 4, 6, and 8 are deficient in small particles (PAH and VSG) while zones 7 and 2 are overabundant. NGC 6357 (zone 2) appears to have the highest X1 value suggesting that shocks can act in addition to the photon flux within NGC 6357. This is consistent with morphology (filamentary structures) of NGC 6357 as seen in Hα.

In the X2 versus R_V plot, a clear split is observed between HII regions (zones 2, 6, and 8) and other regions. These HII regions exhibit a higher X2, while zones 1, 3, 4, 5, and 7 have similar X2 values of around 0.10±0.02. This relative excess emission at 25 μm could mean that there is an excess of VSGs, that the big grain emissivity has been modified (Désert et al. 1990), and/or that the big grain emission contributes significantly to the 25 μm band flux.

[4] IRIS (Improved Reprocessing of the IRAS Survey) data are the improved version of the latest IRAS images, followong the second generation processing (or IRAS Sky Survey Atlas, ISSA). These maps have been reprocessed to improve sensitivity and absolute calibration. Compared to the latest version of the IRAS data, these new images have higher quality zodiacal light subtraction, calibration, and zero level adjustments to match the DIRBE data on large angular scales. The IRIS data have a resolution near 4′ in the four wavelengths (12, 25, 60, and 100 μm).

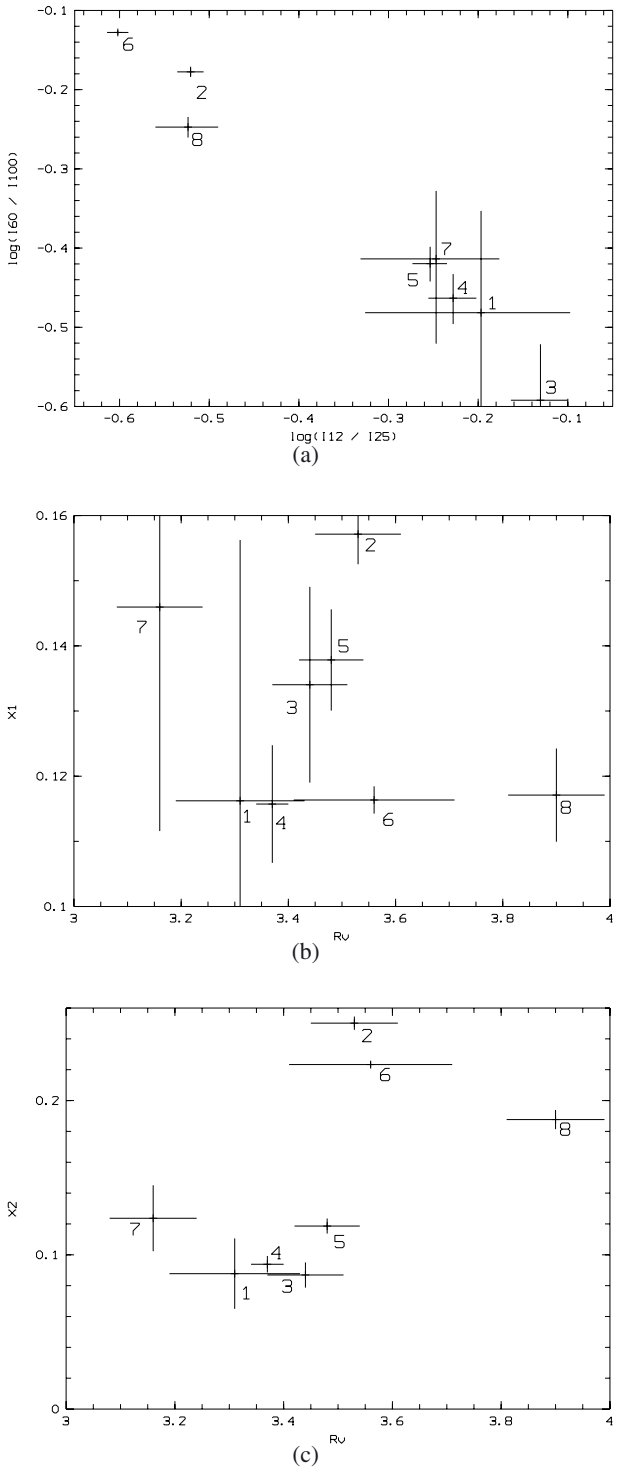

Fig. 5. Far infrared dust emission of the 8 zones. The plots are $\log(I(60)/I(100))$ versus $\log(I(12)/I(25))$ **a)**, X1 versus R_V **b)** and X2 versus R_V **c)**. Labels 2, 6, and 8 correspond to the regions NGC 6357, NGC 6334, and GM24, respectively.

We suggest that there is a global difference between the dust size distributions of NGC 6334 and NGC 6357. The similar R_V in both regions suggests that their big grain content is similar, while NGC 6357 contains more very small grains. The OB stars in NGC 6357 seem then to have already re-processed part of the dust, which could be interpreted as a more evolved status for NGC 6357 than for NGC 6334.

5.4. Galactic structure

The relatively large number of OB stars (Table 3) in our sample allowed us to perform a statistical approach to measuring the stellar distance. The zones exhibit similar star-number surface densities, excepts for zone 4, which has a larger value. This is naturally explained by its location pointing towards the Galactic plane, which naturally probes denser stellar regions. Since from photometric data only it is impossible to determine the luminosity class, when determining the distance we assumed that the stars are main-sequence stars and if this is not the case this leads us to underestimate the distance by up to a factor of 0.6 respectively to class III stars. Taking as a starting point the observed colors $U-B$ and $B-V$, the intrinsic colors $(U-B)_0$ and $(B-V)_0$ and the extinction $A_V = R_V \times E_{B-V}$ are determined following the reddening law and the unreddened main sequence of Schmidt-Kaler (1983). The intrinsic colors are used to determine the spectral type using the main-sequence calibration table of Schmidt-Kaler (1983). The distance is then calculated by adopting the M_V-spectral type calibration from Russeil (2003).

The distance uncertainty is evaluated from the photometric uncertainties as $\sigma_d/d = (\ln(10)/5) \times [\sigma_V + R_V \times \sigma_B + R_V \times \sigma_V + \sigma_{R_V} \times E_{B-V}]$. To determine the distance, we adopted the R_V value of the area where the stars are lying (Fig. 7a).

We considered the U-band completeness level (see Sect. 2.1), assuming a typical diffuse extinction ($A_V = 0.7$ mag kpc^{-1}, Marshall et al. 2006) and a mean extinction of $A_V = 5$ mag at the distance of NGC 6334 – NGC 6357, and taking the absolute U magnitude for a B3V (Schmidt-Kaler 1983) and a O9.5V (Martins & Plez 2006) star we can estimate that we have a 90% mean completeness level for B3V and O9.5V out to 3300 pc and 5000 pc, respectively. At these distances, we can probe the nearest spiral arm structure.

In the model of Russeil et al. (2007), the line of sight in the direction of NGC 6334 – NGC 6357, is expected to cross the Sagittarius-Carina arm at ~1.5 kpc, the Scutum-Crux arm at ~3 kpc, the Norma arm at ~4.3 kpc, and a small feature around 6 kpc. For the Hou et al. (2009) model, the distance to the arms are slightly different: 0.82 kpc, 2.9 kpc and 4.7 kpc for the Sagittarius-Carina, Scutum-Crux, and Norma arms. Figure 7a shows peaks at 1 kpc, 1.8 kpc, 2.6 kpc, and 4.6 kpc. Every peak can be associated with a spiral arm.

To estimate the possible impact of our assumptions about the main-sequence type of the stars, we note (Table 2) that 65% are main sequence stars, 17% are type III stars, and 9% are type I stars. We then repeated our determination of the stellar distance distribution (Fig. 7b) considering these proportions of class V and III and adopting an average factor of 1.5 for the distance of class III stars, respectively, to class V stars. We can discern that the features are globally recovered with peaks at distances of around 1.4, 2.6, and 4.6 kpc.

The average distance of the NGC 6334-NGC 6357 complex (1.75 kpc) places it in the Sagittarius-Carina arm, although it appears to be located slightly farther away than the first stellar peak. Such a configuration was already noted for the other Sagittarius-Carina arm HII region RCW108 (Georgelin et al. 1996) at a distance of 1.4 kpc, while the stellar peak of the field stars is at 1.1 kpc. In parallel, Tovmassian et al. (1996), studying an area of about $12^{\circ 2}$ centered on $l = 297^{\circ}$, $b = -1^{\circ}$ find at the distance of the Sagittarius-Carina arm two separate stellar associations at 1.2 and 1.5 kpc. This suggests that there is a possible branch of the arm or a possible age gradient (with HII regions and field stars located at the far and near edge of the arm). It is most probable that there is a non-zero age gradient across the

Table 3. Mean star number and surface density.

Zone:	1	2	3	4	5	6	7	8
Number:	327	458	409	595	113	199	194	99
Number per $^{\circ 2}$:	346.4	394.8	281.9	1075.9	465.0	314.9	570.6	436.1

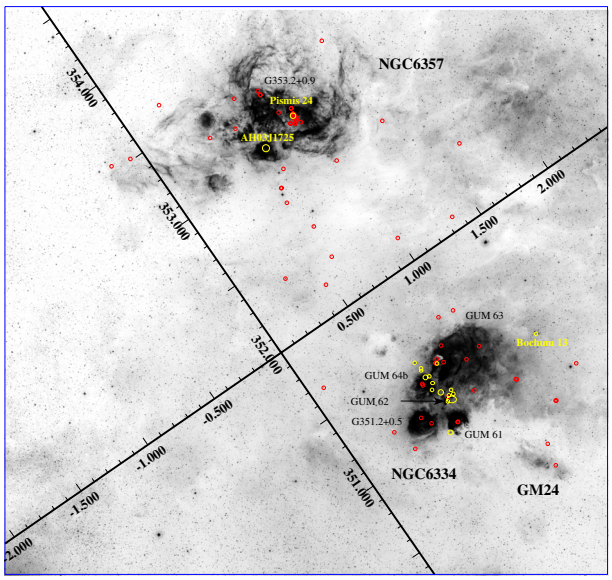

Fig. 6. Hα image (UKST Hα survey, Parker et al. 2005) of the H II regions NGC 6334 and NGC 6357 (Galactic coordinates). The different regions are labeled. Overplotted are the O-B3 stars in the distance range of 1.5 to 1.95 kpc (red circles) and stellar clusters/groups (yellow symbols and names). Clusters/groups without name are clusters from Bica et al. (2003) and Feigelson et al. (2009).

Sagittarius-Carina arm, as Mel'nik et al. (1998) show, because a stratification of stellar ages exists across the Sagittarius-Carina arm, with young objects being located near the inner edge of the arm, while old groupings lie closer to the outer edge.

5.5. The OB stars census

Uncertainty about the first phase of high-mass star formation concerns the relative lengths of the lifetimes of high-mass IR-quiet and high-luminosity protostars as well as prestellar sources detected in submm surveys (Motte et al. 2007). To help resolve this uncertainty, we performed a census of massive stars (earlier than B3) in the NGC 6334-NGC 6357 complex, because the statistical lifetime is measured relative to the known age of OB stars.

The 2.7 GHz radio continuum flux of NGC 6334 and NGC 6357 is 439.4 ± 13.5 Jy and 924.1 ± 29.0 Jy, respectively (fluxes estimated from Paladini et al. 2003). These fluxes correspond to ionising photons fluxes (on a logarithmic scale) of 50.04 s^{-1} and 50.37 s^{-1}. From Table 2, we evaluate the stellar ionising photon flux for both regions using Panagia (1973) and Sternberg et al. (2003). This led to 50.04 s^{-1} and 50.32 s^{-1} for NGC 6334 and NGC 6357, respectively, in good agreement with the radio values and suggests that the main ionizing stars are clearly identified. However, to have a complete census of OB stars we must also consider the OB stars that are not optically visible.

In NGC 6357, two open clusters (Fig. 6) were previously identified, the well-known Pismis 24 and AH03J1726-34.4

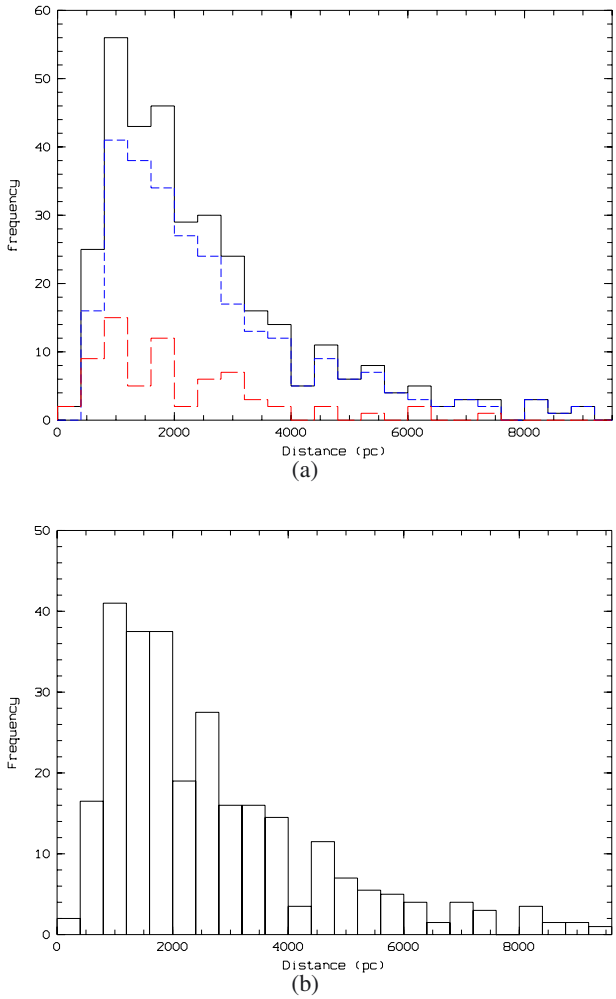

Fig. 7. a) Distribution of distances to OB stars (black histogram). Only stars with distance uncertainties smaller than 400 pc have been considered. The blue dashed histogram is the B star distribution, while the red dashed histogram is the O star distribution. **b)** Distribution of distances to OB stars assuming a proportion of class V and class III stars of 65% and 17%.

(Dias et al. 2002). For Pismis 24, Wang et al. (2007) identified 34 O-B3 stars from X-ray studies. The information on the cluster AH03J1726-34.4 is very sparse. AH03J1726-34.4 contains at least 4 OB stars (Neckel 1984; Damke et al. 2006). We were able to count at least 38 OB stars associated with NGC 6357.

For NGC 6334 (Fig. 6), Neckel (1978) found 14 O-B3 stars from optical photometry, and Bica et al. (2003) listed 7 embedded clusters/groups associated with radio sources. Feigelson et al. (2009) show (from a X-ray census of stellar sources in NGC 6334) a complicated spatial pattern with ∼10 distinct star clusters (the heavily obscured clusters are mostly associated with known far-infrared sources and radio H II regions). They also found dozens of likely OB stars, both in clusters, and dispersed throughout the region, suggesting that star formation in the complex has proceeded over millions of years. Tapia et al. (1996)

deduced that the young cluster embedded in NGC 6334I has around 93 stars members brighter than $K = 16$ and that the majority of the observed members are ZAMS stars earlier than B3-B4. Tapia et al. (1996) found 12 faint sources (detected only in K band) centered on the HII region NGC 6334E. They estimated that the ionization of NGC 6334E requires at least an O7.5 ZAMS star or 12-13 B0-B0.5 ZAMS stars. They then proposed that a cluster of B stars is responsible for the ionization of NGC 6334E. Bochum 13, a cluster at the north-west border of NGC 6334, and at the same distance, contains 5 O-B3 stars (McSwain 2005) and a cluster dominated by a few young massive stars (∼10) lies in the core of GM24 (Tapia et al. 1991). We then count at least 150 OB stars associated with NGC 6334.

Our UBV data provide an estimate of 40 additional optically visible O-B3 stars at the distance of NGC 6334-NGC 6357 complex (Fig. 6), giving a total count of at least 228 OB stars. We can thus estimate that 230 massive stars (earlier than B3) belong to the entire complex.

In Russeil et al. (2010), we presented a census of high-mass young stellar objects at various evolutionary stages: we identified 1 starless clump, 6 IR-quiet protostars, and 9 high-luminosity IR protostars in NGC 6334-NGC 6357. Since the timescale of the high-mass young objects cannot be derived directly, a statistical method was used. Assuming a steady star formation, the ratio of the number of objects at each stage is proportional to the stage timescale. The unit of time was estimated from the number and age of OB stars. The adopted age of OB stars in NGC 6334-NGC 6357 comes from the age of the cluster Pismis 24, which is between 1.73 Myr (Massey et al. 2001) and 5 ± 3 Myr (Ahumada et al. 2007). This means that from our number of ∼230 OB stars, one high-mass young object corresponds to a statistical lifetime of between $\sim 7.5 \times 10^3$ yr and $\sim 2.2 \times 10^4$ yr. We can then, in NGC 6334-NGC 6357, estimate that the starless and the protostellar phases have a statistical lifetime of $7.5 \times 10^3 - 2.2 \times 10^4$ yr and $1.1 \times 10^5 - 3.3 \times 10^5$ yr, respectively.

6. Conclusions

The results that we have presented in this paper stress the effectiveness of multicolor optical photometry in the study of the extinction and distance towards HII regions. Our large stellar sample has allowed us to carry out a statistical study of the local structure of the Milky-Way, as well as the census of O-B3 stars in the NGC 6334-NGC 6357 star-forming complex. Spectroscopic information of our large O-B3 stellar sample is now required to confirm the photometric spectral types and improve our distance determinations.

As expected, the total-to-selective extinction coefficient, R_V, is higher in a star-forming region such as NGC 6334-NGC 6357 than in the diffuse interstellar medium. Futhermore, this coefficient varies throughout the HII regions, suggesting that there is a variation in the dust properties on the same scale. The R_V values we obtained for NGC 6334 and NGC 6357 (3.56 ± 0.15 and 3.53 ± 0.08, respectively) have allowed us to determine more precisely the distance of these regions. We have confirmed that they are located at an average distance of 1.75 kpc. Our census of O-B3 stars in the NGC 6334-NGC 6357 star-forming complex has identified a total of 300 O-B3 stars. This census is important to help us to determine the statistical lifetimes of the different stages of the high-mass star formation in NGC 6334-NGC 6357 that we observe in the infrared with the *Herschel* satellite (Russeil et al., in prep.).

Acknowledgements. Part of this work was supported by the ANR (Agence Nationale pour la recherche) project "PROBES", number ANR-08-BLAN-0241. Part of this work was completed thanks to SIMBAD and CDS. The authors acknowledge D. Clowe and M. P. Ulmer, respectively PI and Co-I of the NOAO observing time (NOAO 2009A-0137), and L. Guennou for their implication in the NOAO observations.

References

Adami, C., Picat, J. P., Savine, C., et al. 2006, A&A, 451, 1159
Ahumada, A., Claría, J., & Bica, E. 2007, A&A, 473, 437
Bertelli, G., Bressan, A., Chiosi, C., et al. 1994, A&AS, 106, 275
Bertin, E., & Arnouts, S. 1996, A&AS, 117, 393
Bertin, E., Mellier, Y., & Radovich, M. 2002, ASPC, 281, 228
Bica, E., Dutra, C., & Barbuy, B. 2003, A&A, 397, 177
Bohigas, J., Tapia, M., Roth, M., et al. 2004, AJ, 127, 2826
Boulanger, F., Beuchman, C., Désert, F., et al. 1988, ApJ, 332, 328
Cardelli, J. A., Clayton, G. C., & Mathis, J. S. 1989, ApJ, 345, 245
Carey, S., Noriega-Crespo, A., & Mizuno, D. 2009, PASP, 121, 76
Carpenter, J. 2001, AJ, 121, 2851
Caswell, J., & Haynes, R. 1987, A&A, 171, 261
Chini, R., & Kruegel, E. 1983, A&A, 117, 289
Chini, R., & Wargau, W. 1990, A&A, 227, 213
Chini, R., Elsasser, H., & Neckel, T. 1980, A&A, 91, 186
Conti, P., & Vacca, W. 1990, AJ, 100, 431
Curti, R., et al. 2003, 2MASS All-Sky Point Sources (Pasadena: NASA/IPAC), http://iras.ipac.caltech.edu/applications/Gator
Damke, G., Barba, R., & Morrell, N. 2006, Rev. Mex. Astron. Astrofis., 26, 180
de Grijs, R., O'Connell, R. W., & Gallagher, J. S. 2001, AJ, 121, 768
Désert, F., Boulanger, F., & Puget, J. L. 1990, A&A, 237, 215
Dias, W., Alessi, B., Moitinho, A., et al. 2002, A&A, 389, 871
Durret, F., Laganá, T. F., Adami, C., & Bertin, E. 2010, A&A, 517, A94
Epchtein, N., de Batz, B., Capoani, L., et al. 1997, Msngr, 87, 27
Fang, X., Storey, P. J., & Liu, X.-W. 2011, A&A, 530, A18
Feigelson, E., Martin, A., McNeill, C., et al. 2009, AJ, 138, 227
Fitzpatrick, E. L. 2004, ASPC, 309, 33
Georgelin, Y. M., Russeil, D., Marcelin, M., et al. 1996, A&AS, 120, 41
Greve, A. 2010, A&A, 518, A62
Gum, C. S. 1955, MmRAS, 67, 155
Gyulbudaghian, A., & Maghakian, T. 1977, PAZh, 3, 113
Hanson, M., Howarth, I., & Conti, P. 1997, ApJ, 489, 698
Heiles, C., Reach, W., & Koo, B. 1988, ApJ, 332, 313
Hou, L. G., Han, J. L., & Shi, W. B. 2009, A&A, 499, 473
Jones, A. 2005, Proc. The dusty and Molecular Universe, ESAP, 577, 239
Koornneef, J. 1983, A&A, 128, 84
Kraemer, K., & Jackson, J. 1999, ApJS, 124, 439
Kroupa, P. 2001, MNRAS, 322, 231
Landolt, A. U. 2009, AJ, 137, 4186
Leitherer, C. 1999, Spectrophotometric Dating of Stars and Galaxies, ed. I. Hubeny, S. Heap, & R. Cornett, ASP Conf. Proc., 192, 3
Lortet, M., Testor, G., & Niemela, V. 1984, A&A, 140, 24
Marshall, D. J., Robin, A. C., Reylé, C., et al. 2006, A&A, 453, 635
Martins, F., & Plez, B. 2006, A&A, 457, 637
Massey, P., DeGioia-Eastwood, K., & Waterhouse, E. 2001, AJ, 121, 1050
Mazzei, P., & Barbaro, G. 2008, MNRAS, 390, 706
Mazzei, P., & Barbaro, G. 2011, A&A, 527, A34
Mel'nik, A., Sitnik, T., Dambis, A., et al. 1998, AstL, 24, 594
Moffat, A., & Vogt, N. 1973, A&AS, 10, 135
Monet, F., Levine, S. E., Canzian, B., et al. 2003, AJ, 125, 98
Motte, F., Bontemps, S., Schilke, P., et al. 2007, A&A, 476, 1243
Neckel, T. 1978, A&A, 69, 51
Neckel, Th. 1984, A&A, 137, 58
Neckel, Th., & Chini, R. 1981, A&AS, 45, 451
O'Dell, C. R., & Wen, Z. 1992, ApJ, 387, 229
Paladini, R., Burigana, C., & Davies, R. 2003, A&A, 397, 213
Panagia, N. 1973, AJ, 78, 929
Pandey, A., Ogura, K., & Sekiguchi, K. 2000, PASJ, 52, 847
Pandey, A., Upadhyay, K., Nakada, Y., et al. 2003, A&A, 397, 191
Parker, Q., Phillipps, S., Pierce, M., et al. 2005, MNRAS, 362, 689
Persi, P., & Tapia, M. 2008, Handbook of Star Forming Regions, Vol. II: The Southern Sky ASP Monograph Publications, ed. B. Reipurth, 5, 456
Pinheiro, M., Copetti, M., & Oliviera, V. 2010, A&A, 521, A26
Rieke, G., & Lebofsky, M. 1985, ApJ, 288, 618
Roslund, C. 1966, Arkiv. Astr., 4, 101
Russeil, D. 2003, A&A, 397, 133
Russeil, D., Adami, C., & Georgelin, Y. M. 2007, A&A, 470, 161
Russeil, D., Zavagno, A., Motte, F., et al. 2010, A&A, 515, A55

Russeil, D., Pestalozzi, M., Mottram, J. C., et al. 2011, A&A, 526, A151
Samal, M., Pandey, A., Ojha, D., et al. 2007, ApJ, 671, 555
Schmidt Kaler, Th. 1983, Landolt-Bornstein, New Series, Group VI (Springer), 23, 14
Seab, C., & Shull, J. 1983, ApJ, 275, 652
Skrutskie, M. F., Cutri, R. M., & Stiening, R. 2006, AJ, 131, 1163
Sternberg, A., Hoffmann, T., & Pauldrach, A. 2003, ApJ, 599, 1333
Tapia, M., Roth, M., Lopez, J., et al. 1991, A&A, 242, 388
Tapia, M., Persi, P., & Roth, M. 1996, A&A, 316, 102
Tovmassian, H., Navarro, S., & Cardona, O. 1996, AJ, 111, 306
Tovmassian, H., Epremian, R., Hovhannessian, R., et al. 1998, AJ, 115, 1083
Turner, D. 1989, AJ, 98, 2300
Turner, D. 1996, AJ, 111, 828
McSwain, M., & Gies, D. 2005, ApJS, 161, 118
Van der Hucht, K. 2001, NewAR, 45, 135
Walborn, N. 1982, AJ, 87, 1300
Wang, J., Townsley, L., Feigelson, E., et al. 2007, ApJS, 168, 100
Wegner, W. 1993, AcA, 43, 209
Wegner, W. 1994, MNRAS, 270, 229
Whittet, D. C. B 2003, Dust in the Galactic Environment, 2nd edn. (Bristol: Institute of Physics (IOP) Publishing), Series in Astronomy and Astrophysics
Whittet, D., & van Breda, I. 1978, A&A, 66, 57
Whittet, D., & van Breda, I. 1980, MNRAS, 192, 467
Whittet, D., van Breda, I., & Glass, I. 1976, MNRAS, 177, 625

Pages 12 to 21 are available in the electronic edition of the journal at http://www.aanda.org

Appendix A: Presentation of the data

Tables presenting the data are given in this section.

Table A.1. Stars with U, B, and V magnitudes.

RA (J2000)	Dec (J2000)	RA °	Dec °	V mag	σ_V mag	B mag	σ_B mag	U mag	σ_U mag
17:22:17.4	−35:43:08.3	260.572	−35.718	17.372	0.017	19.034	0.032	19.987	0.118
17:22:20.5	−35:40:28.4	260.585	−35.674	13.315	0.003	14.292	0.004	14.845	0.011
17:22:19.2	−35:38:29.9	260.580	−35.641	18.374	0.026	20.041	0.053	21.203	0.218
17:22:20.9	−35:39:45.1	260.587	−35.662	15.223	0.006	16.536	0.010	17.275	0.033
17:22:20.1	−35:43:17.1	260.583	−35.721	18.679	0.030	20.486	0.067	21.369	0.245
17:22:20.5	−35:41:50.2	260.585	−35.697	18.850	0.033	20.728	0.077	21.744	0.294
17:22:21.2	−35:37:04.3	260.588	−35.617	16.900	0.013	18.833	0.029	20.876	0.181
17:22:21.9	−35:38:24.5	260.591	−35.640	15.986	0.009	17.505	0.016	18.351	0.054
17:22:22.4	−35:42:16.1	260.593	−35.704	18.399	0.027	20.231	0.059	22.059	0.334
...	...	...	...	...	...	...	...	...	...

Notes. The full table is available at the CDS.

Table A.2. Catalogue of stars: R magnitudes.

RA (J2000)	Dec (J2000)	RA °	Dec °	R mag	σ_R mag
17:24:20.9	−33:58:13.1	261.087	−33.970	13.720	0.021
17:24:41.5	−34:11:04.9	261.173	−34.184	13.726	0.021
17:26:16.8	−33:55:58.8	261.570	−33.933	13.754	0.021
17:25:25.4	−34:30:35.3	261.356	−34.509	13.762	0.021
17:24:07.0	−33:56:26.9	261.029	−33.940	13.774	0.021
17:25:03.8	−33:56:31.2	261.266	−33.942	13.779	0.021
17:24:16.3	−34:10:22.8	261.068	−34.173	13.795	0.015
17:26:37.4	−34:23:39.5	261.656	−34.394	13.798	0.021
17:24:18.7	−34:20:27.6	261.078	−34.341	13.801	0.021
...	...	...	...	...	...

Notes. The full table is available at the CDS.

Appendix B: The results

We present the results of the fits and all the two-color diagrams for zones 1 to 8. Table B.1 gives the slope of the linear regression for the different filters in the 8 zones. The normal slope is given in the last row. For a few zones and a few wavelengths, it is impossible to determine any reliable slope because of the too small number of data points. Table B.2 gives the correlation coefficient of the fit. Table B.3 gives the R_V values deduced from Eq. (1). The last column gives the R_V weighted mean value. The small thick segment at the bottom left of the plots is the locus of the unreddened O-B3 stars (from Martins et al. 2006; Koornneef et al. 1983; and Wegner 1994).

Table B.1. Fitted slopes.

Zone	$\frac{V-R}{B-V}$ CTIO	$\frac{V-R}{B-V}$ USNO	$\frac{V-I}{B-V}$ USNO	$\frac{V-I}{B-V}$ DENIS	$\frac{V-J}{B-V}$ DENIS	$\frac{V-K}{B-V}$ DENIS	$\frac{V-J}{B-V}$ 2MASS	$\frac{V-H}{B-V}$ 2MASS	$\frac{V-K}{B-V}$ 2MASS
1		0.64 ± 0.12	1.34 ± 0.12	0.75 ± 0.17	2.17 ± 0.11	2.98 ± 0.66	2.22 ± 0.27	2.48 ± 0.58	2.35 ± 0.30
2	1.02 ± 0.11	0.86 ± 0.13	1.49 ± 0.20	1.17 ± 0.07	2.23 ± 0.14	2.98 ± 0.19	2.19 ± 0.13	2.78 ± 0.13	2.83 ± 0.15
3	0.73 ± 0.07	0.82 ± 0.07	1.33 ± 0.14	1.22 ± 0.06	2.21 ± 0.11	2.80 ± 0.57	2.19 ± 0.10	2.49 ± 0.13	2.71 ± 0.15
4		0.74 ± 0.04	1.38 ± 0.05	1.24 ± 0.03	2.17 ± 0.04	2.73 ± 0.10	2.21 ± 0.05	2.52 ± 0.04	2.70 ± 0.06
5		0.84 ± 0.10	1.36 ± 0.17	1.30 ± 0.04	2.31 ± 0.10	2.62 ± 0.17	2.21 ± 0.15	2.41 ± 0.15	2.65 ± 0.13
6	0.82 ± 0.08		0.94 ± 0.17	1.45 ± 0.13	2.43 ± 0.32	2.98 ± 0.37	2.30 ± 0.26	2.24 ± 0.29	2.72 ± 0.38
7			1.17 ± 0.09	1.47 ± 0.06	2.16 ± 0.45	2.58 ± 0.49	2.07 ± 0.44	2.43 ± 0.78	2.29 ± 0.09
8			1.63 ± 0.44	1.56 ± 0.08	2.75 ± 0.21	3.16 ± 0.21	2.60 ± 0.11	2.71 ± 0.16	2.91 ± 0.18
normal	0.55	0.55	1.10	1.10	1.96	2.60	1.96	2.42	2.60

Table B.2. Correlation coefficient of the fitted lines.

Zone	$\frac{V-R}{B-V}$ CTIO	$\frac{V-R}{B-V}$ USNO	$\frac{V-I}{B-V}$ USNO	$\frac{V-I}{B-V}$ DENIS	$\frac{V-J}{B-V}$ DENIS	$\frac{V-K}{B-V}$ DENIS	$\frac{V-J}{B-V}$ 2MASS	$\frac{V-H}{B-V}$ 2MASS	$\frac{V-K}{B-V}$ 2MASS
1		0.50	0.89	0.60	0.88	0.77	0.87	0.61	0.84
2	0.90	0.71	0.67	0.87	0.88	0.89	0.88	0.93	0.90
3	0.96	0.83	0.72	0.89	0.89	0.78	0.92	0.90	0.74
4		0.86	0.93	0.97	0.98	0.98	0.97	0.98	0.97
5		0.81	0.81	0.97	0.97	0.98	0.92	0.93	0.69
6	0.98		0.85	0.95	0.90	0.93	0.93	0.89	0.89
7			0.99	0.99	0.90	0.91	0.92	0.80	0.99
8			0.80	0.98	0.97	0.98	0.97	0.95	0.95

Table B.3. R_V determination.

Zone	$\frac{V-R}{B-V}$ CTIO	$\frac{V-R}{B-V}$ USNO	$\frac{V-I}{B-V}$ USNO	$\frac{V-I}{B-V}$ DENIS	$\frac{V-J}{B-V}$ DENIS	$\frac{V-K}{B-V}$ DENIS	$\frac{V-J}{B-V}$ 2MASS	$\frac{V-H}{B-V}$ 2MASS	$\frac{V-K}{B-V}$ 2MASS	Weighted mean value
1		3.55 ± 0.68	3.78 ± 0.34	2.11 ± 0.48	3.43 ± 0.17	3.55 ± 0.79	3.51 ± 0.43	3.18 ± 0.74	2.80 ± 0.36	3.32 ± 0.12
2	5.75 ± 0.62	4.85 ± 0.73	4.20 ± 0.56	3.30 ± 0.20	3.53 ± 0.22	3.55 ± 0.23	3.46 ± 0.21	3.56 ± 0.17	3.37 ± 0.18	3.53 ± 0.08
3	4.11 ± 0.39	4.62 ± 0.39	3.75 ± 0.39	3.44 ± 0.17	3.50 ± 0.17	3.34 ± 0.68	3.46 ± 0.16	3.19 ± 0.17	3.23 ± 0.18	3.44 ± 0.07
4		4.17 ± 0.28	3.89 ± 0.14	3.49 ± 0.08	3.43 ± 0.06	3.26 ± 0.12	3.5 ± 0.08	3.23 ± 0.05	3.22 ± 0.07	3.37 ± 0.03
5		4.73 ± 0.56	3.83 ± 0.48	3.66 ± 0.11	3.65 ± 0.16	3.12 ± 0.2	3.50 ± 0.24	3.09 ± 0.19	3.16 ± 0.16	3.46 ± 0.06
6	4.62 ± 0.45		2.65 ± 0.48	4.09 ± 0.37	3.84 ± 0.51	3.55 ± 0.44	3.64 ± 0.41	2.87 ± 0.37	3.24 ± 0.45	3.56 ± 0.15
7			3.30 ± 0.25	4.14 ± 0.17	3.42 ± 0.71	3.08 ± 0.58	3.27 ± 0.70	3.11 ± 1.0	2.73 ± 0.11	3.16 ± 0.08
8			4.59 ± 1.24	4.40 ± 0.23	4.35 ± 0.33	3.77 ± 0.25	4.11 ± 0.17	3.47 ± 0.2	3.47 ± 0.21	3.89 ± 0.09

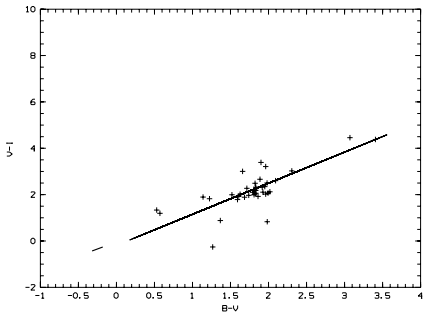

(a) V - (USNO I) vs. B-V

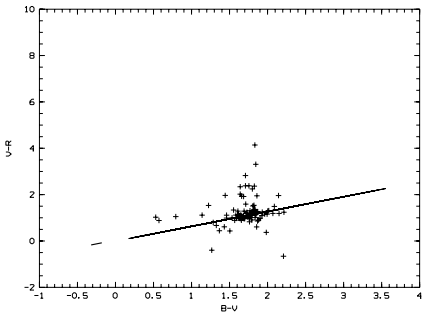

(b) V - (USNO R) vs. B-V

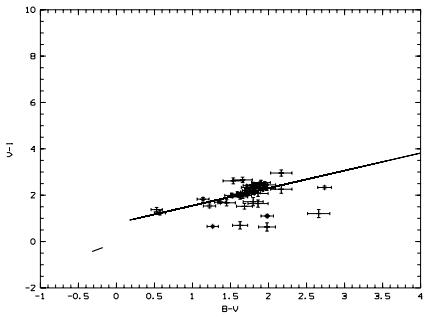

(c) V - (DENIS I) vs. B-V

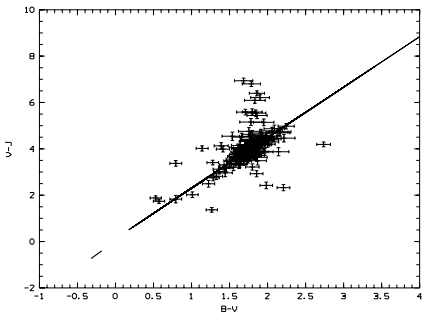

(d) V - (DENIS J) vs. B-V

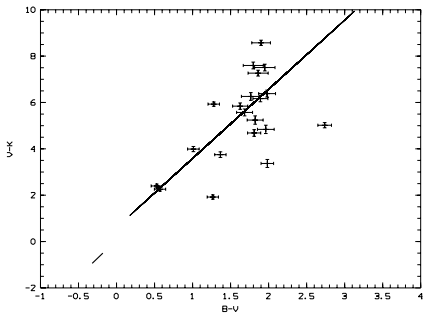

(e) V - (DENIS K_S) vs. B-V

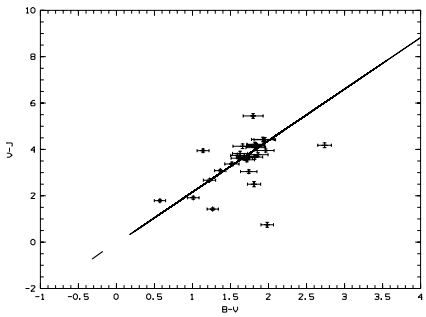

(f) V - (2MASS J) vs. B-V

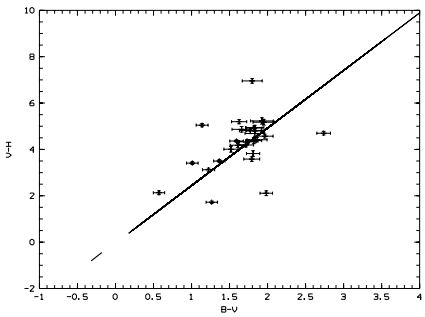

(g) V - (2MASS H) vs. B-V

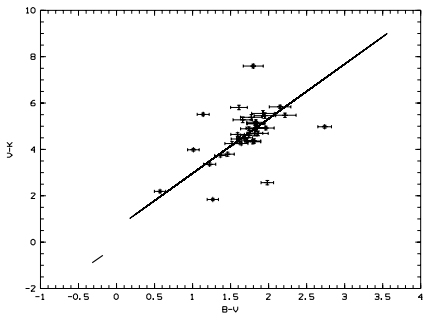

(h) V - (2MASS K_S) vs. B-V

Fig. B.1. Zone 1 two color diagrams.

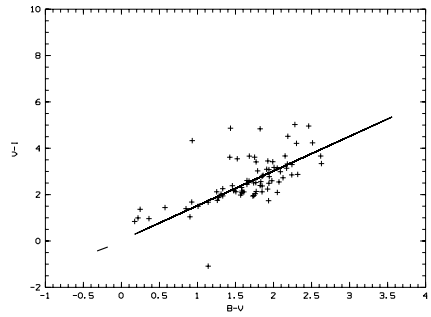

(a) V - (USNO I) vs. B-V

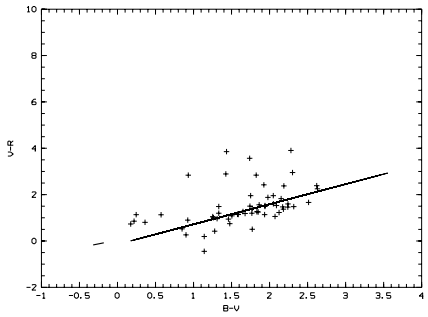

(b) V - (USNO R) vs. B-V

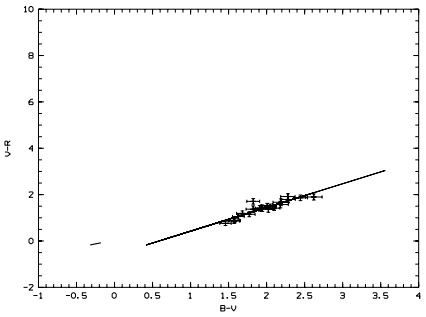

(c) V - (CTIO R) vs. B-V

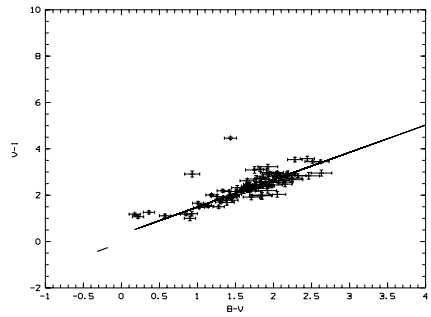

(d) V - (DENIS I) vs. B-V

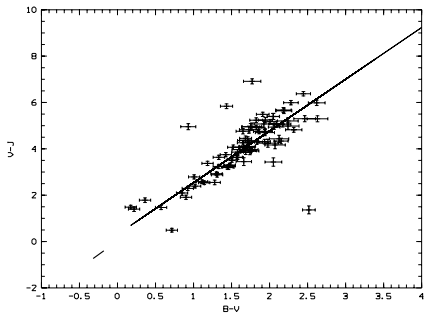

(e) V - (DENIS J) vs. B-V

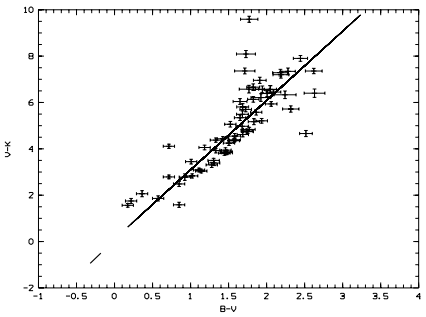

(f) V - (DENIS K_S) vs. B-V

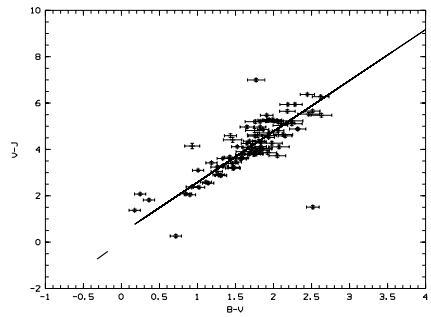

(g) V - (2MASS J) vs. B-V

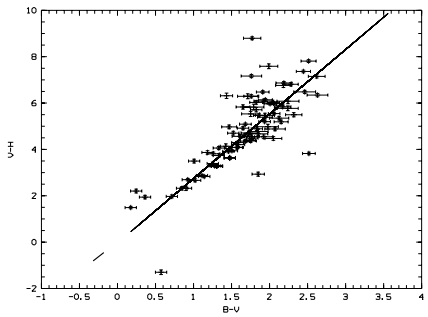

(h) V - (2MASS H) vs. B-V

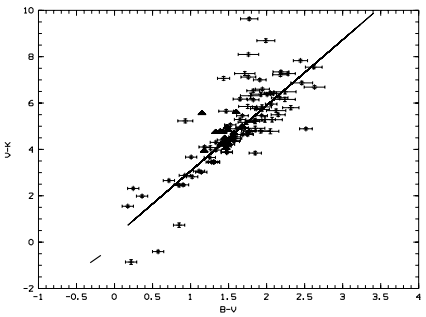

(i) V - (2MASS K_S) vs. B-V

Fig. B.2. Zone 2 two color diagrams.

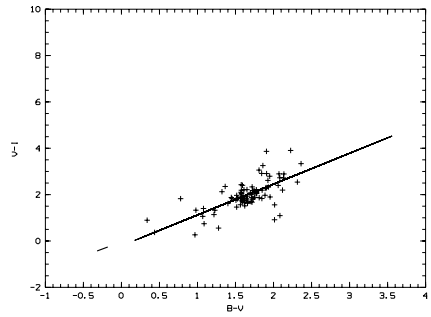

(a) V - (USNO I) vs. B-V

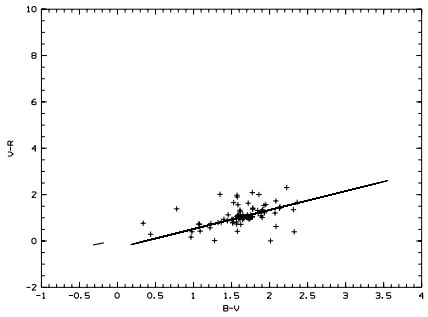

(b) V - (USNO R) vs. B-V

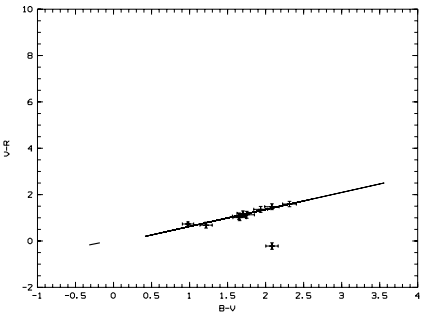

(c) V - (CTIO R) vs. B-V

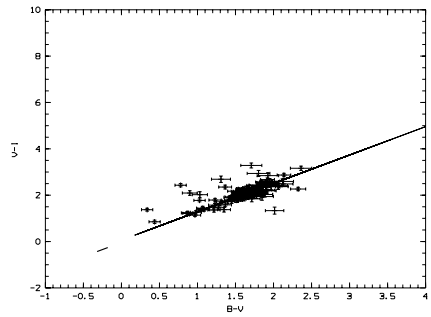

(d) V - (DENIS I) vs. B-V

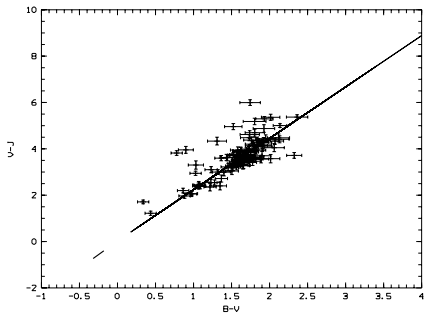

(e) V - (DENIS J) vs. B-V

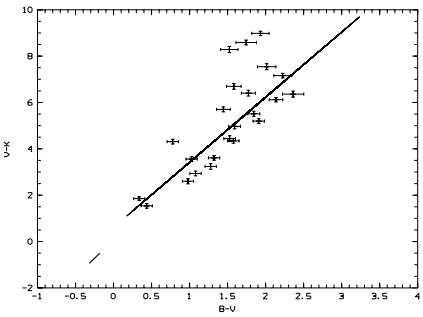

(f) V - (DENIS K_S) vs. B-V

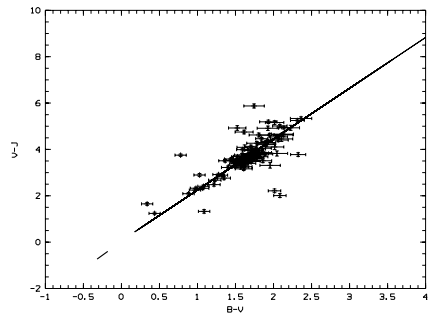

(g) V - (2MASS J) vs. B-V

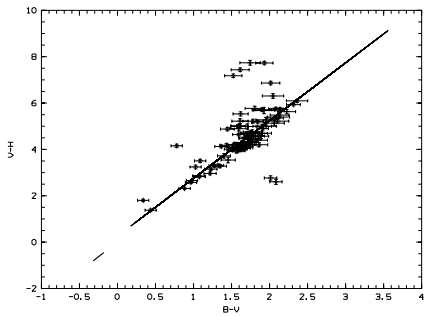

(h) V - (2MASS H) vs. B-V

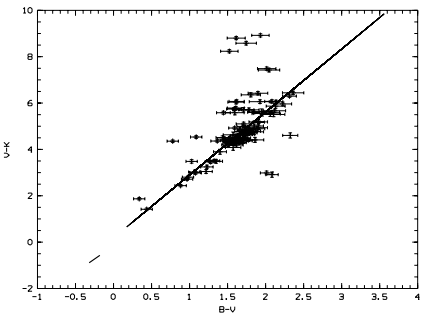

(i) V - (2MASS K_S) vs. B-V

Fig. B.3. Zone 3 two color diagrams.

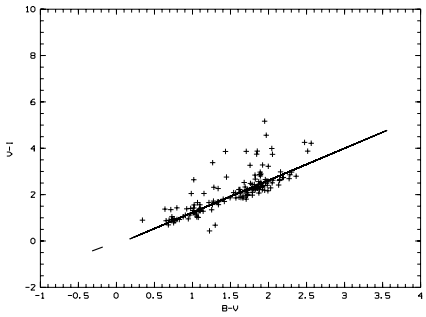

(a) V - (USNO I) vs. B-V

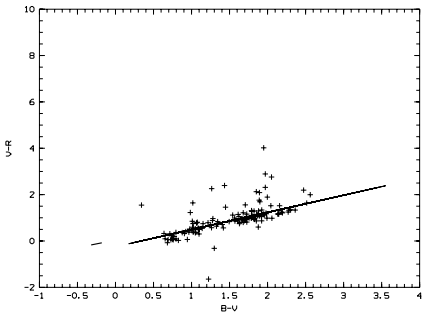

(b) V - (USNO R) vs. B-V

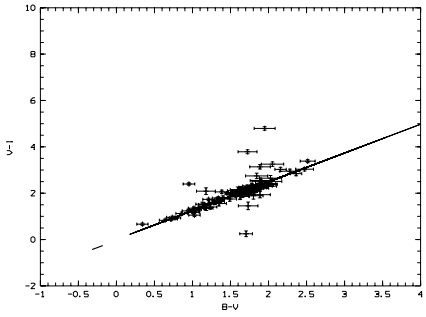

(c) V - (DENIS I) vs. B-V

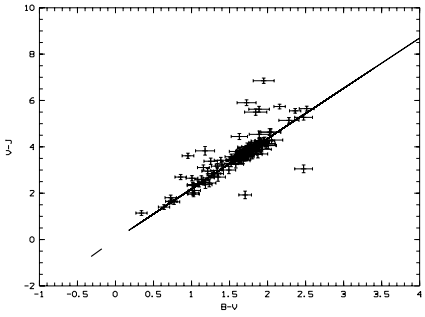

(d) V - (DENIS J) vs. B-V

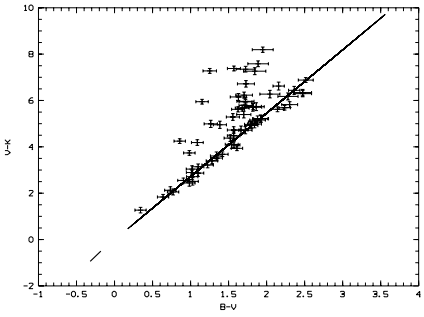

(e) V - (DENIS K_S) vs. B-V

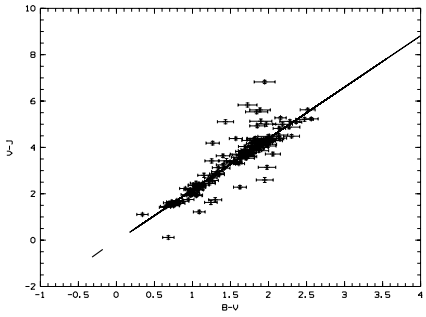

(f) V - (2MASS J) vs. B-V

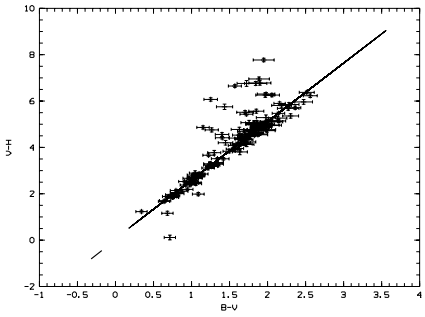

(g) V - (2MASS H) vs. B-V

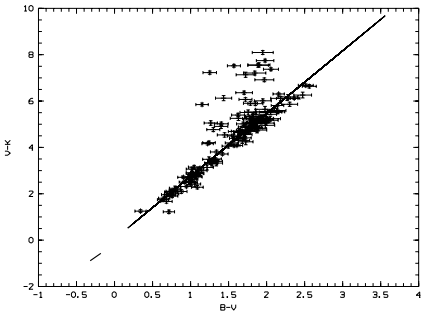

(h) V - (2MASS K_S) vs. B-V

Fig. B.4. Zone 4 two color diagrams.

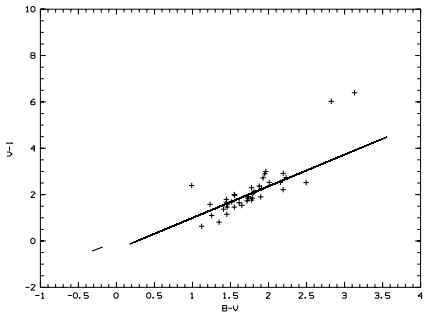

(a) V - (USNO I) vs. B-V

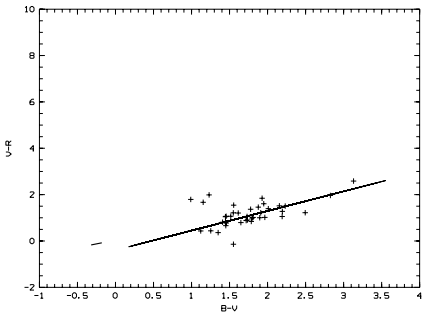

(b) V - (USNO R) vs. B-V

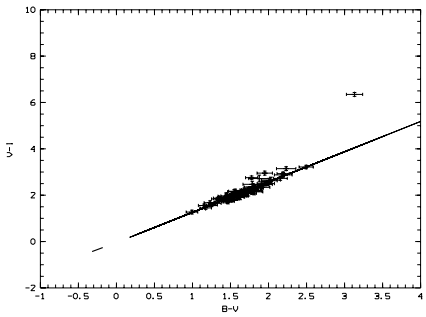

(c) V - (DENIS I) vs. B-V

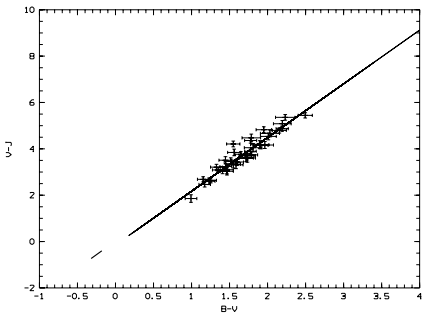

(d) V - (DENIS J) vs. B-V

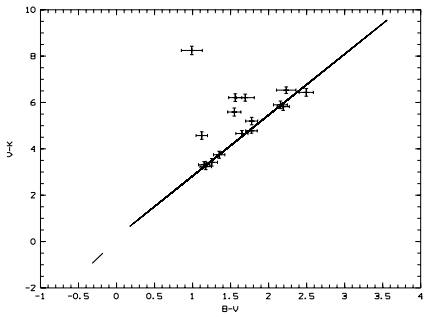

(e) V - (DENIS K_S) vs. B-V

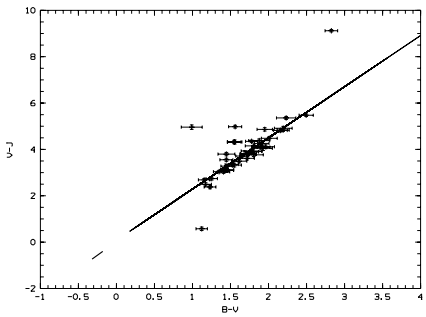

(f) V - (2MASS J) vs. B-V

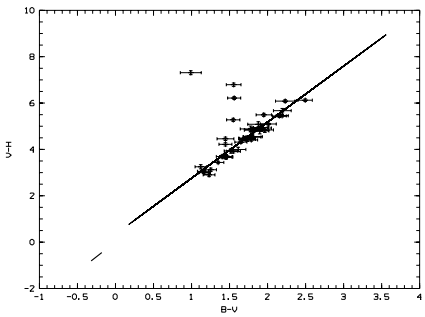

(g) V - (2MASS H) vs. B-V

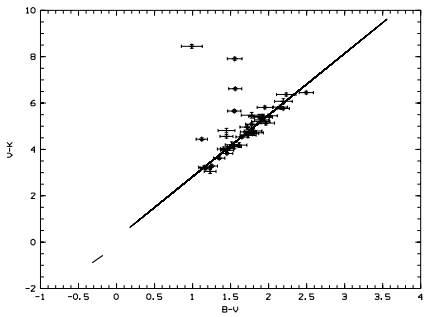

(h) V - (2MASS K_S) vs. B-V

Fig. B.5. Zone 5 two color diagrams.

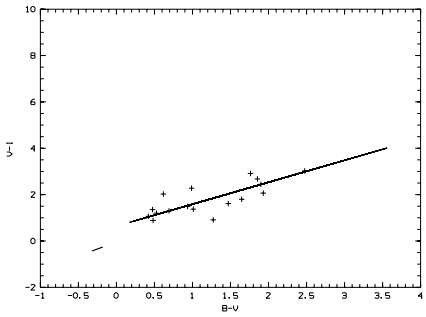

(a) V - (USNO I) vs. B-V

(b) V - (USNO R) vs. B-V

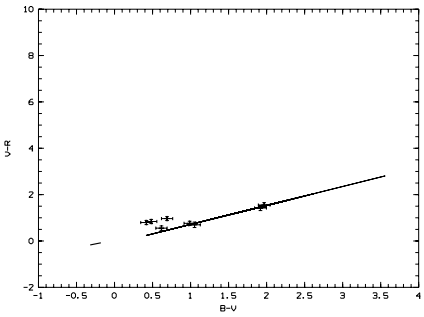

(c) V - (CTIO R) vs. B-V

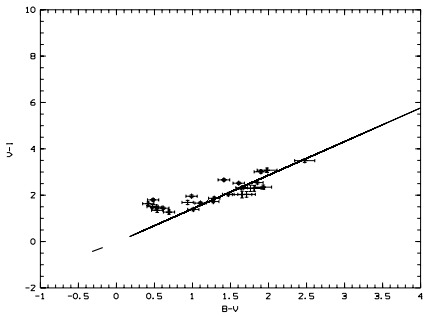

(d) V - (DENIS I) vs. B-V

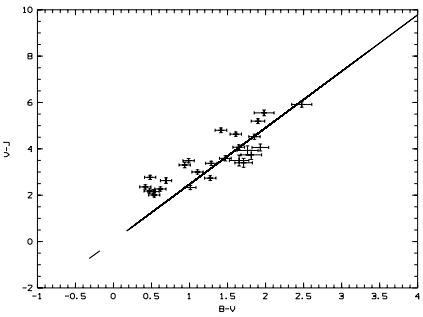

(e) V - (DENIS J) vs. B-V

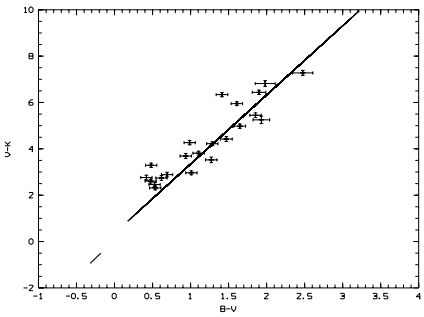

(f) V - (DENIS K_S) vs. B-V

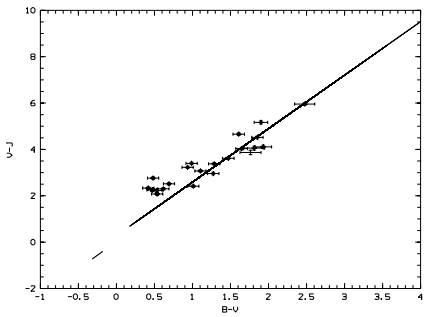

(g) V - (2MASS J) vs. B-V

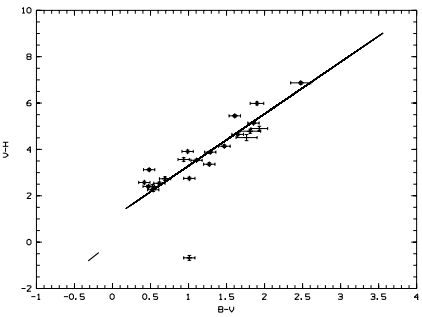

(h) V - (2MASS H) vs. B-V

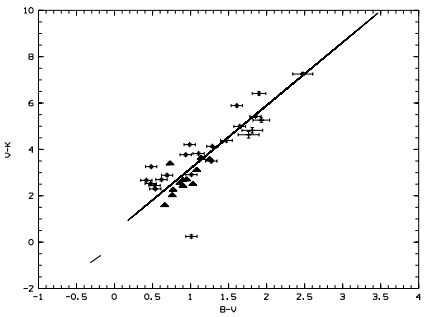

(i) V - (2MASS K_S) vs. B-V

Fig. B.6. Zone 6 two color diagrams.

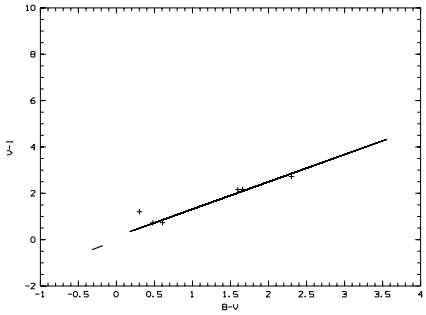

(a) V - (USNO I) vs. B-V

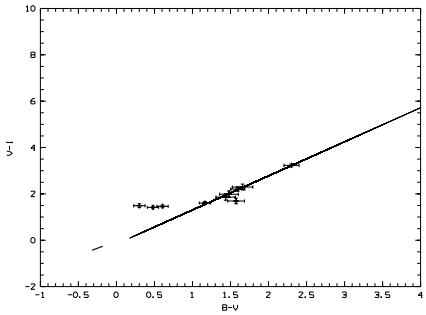

(b) V - (DENIS I) vs. B-V

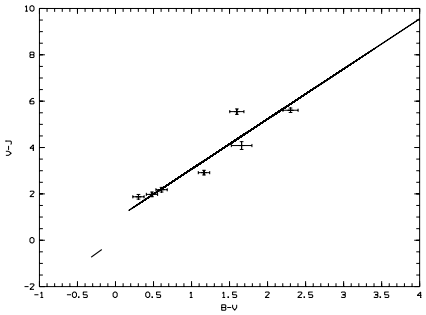

(c) V - (DENIS J) vs. B-V

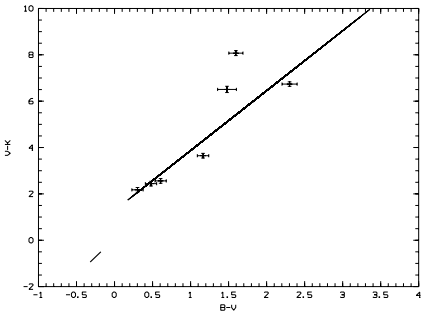

(d) V - (DENIS K_S) vs. B-V

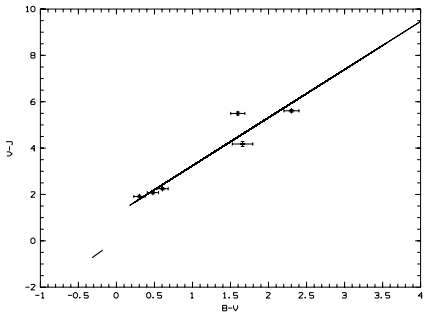

(e) V - (2MASS J) vs. B-V

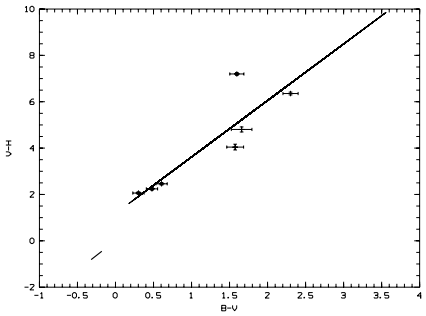

(f) V - (2MASS H) vs. B-V

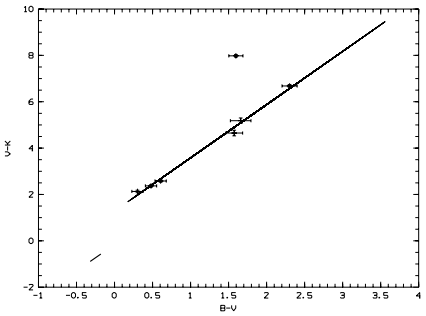

(g) V - (2MASS K_S) vs. B-V

Fig. B.7: Zone 7 two color diagrams.

Fig. B.7. Zone 7 two color diagrams.

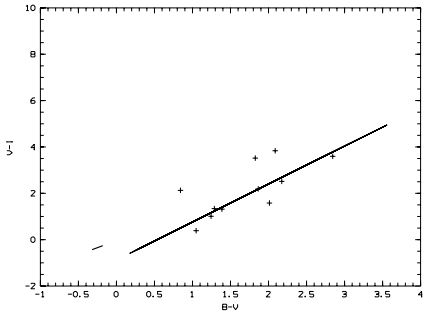

(a) V - (USNO I) vs. B-V

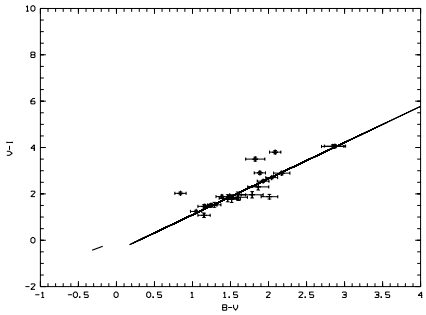

(b) V - (DENIS I) vs. B-V

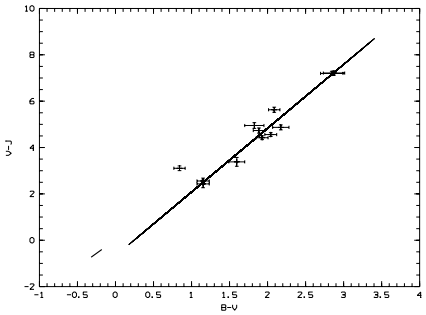

(c) V - (DENIS J) vs. B-V

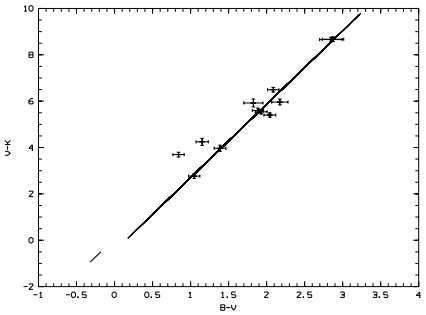

(d) V - (DENIS K_S) vs. B-V

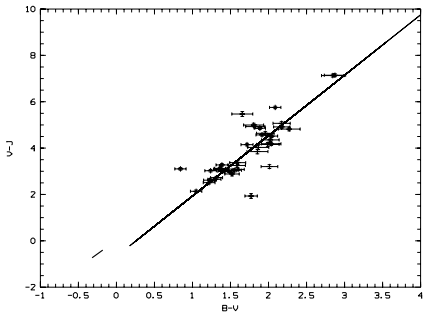

(e) V - (2MASS J) vs. B-V

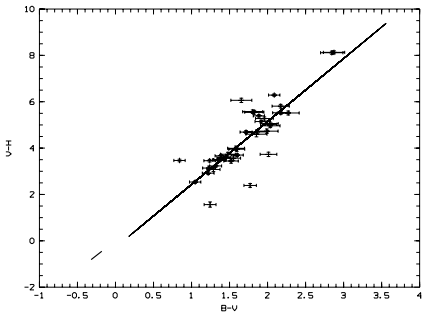

(f) V - (2MASS H) vs. B-V

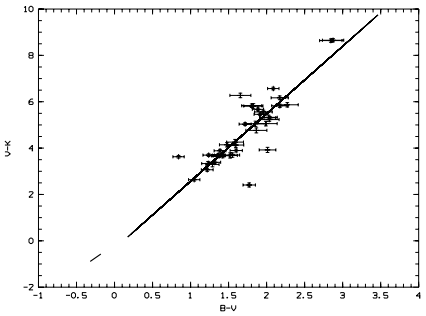

(g) V - (2MASS K_S) vs. B-V

Fig. B.8: Zone 8 two color diagrams.

Fig. B.8. Zone 8 two color diagrams.